Terahertz Conductivity Measurements of MnSi

by

Laleh Mohtashemi
B.Sc. (Hons.), Simon Fraser University, 2011

A Thesis submitted in partial fulfillment
of the requirements for the degree of

Master of Science

in the
Department of Physics
Faculty of Science

SIMON FRASER UNIVERSITY
Fall 2013

Approval

Name: **Laleh Mohtashemi**

Degree: **Master of Science (Physics)**

Title of the thesis: ***THz Conductivity Measurements of MnSi***

Examining Committee:

Chair: John Bechhoefer, Professor

J. Steve Dodge
Senior Supervisor
Associate Professor

Malcolm Kennett
Supervisor
Associate Professor

David Broun
Internal Examiner
Associate Professor

Date Defended/Approved: **Dec 18, 2013**

Partial Copyright Licence

Abstract

This thesis presents measurements of the dynamical conductivity of a MnSi film via terahertz time domain spectroscopy. We determine the Drude scattering rate and plasma frequency at low temperatures, and compare these to theoretical predictions. From a comparison of the plasma frequency measurement with band theory, we determine a mass renormalization of $m^*/m \simeq 5.5$. Above $T_c = 50$ K, fits to the Drude model yield negative values for τ, indicating the existence of a pseudogap. At low temperatures and low frequencies, the resistivity has the form $\rho(\omega, T) = A\left[(\hbar\omega)^2 + b(\pi k_B T)^2\right]$, with $b \gtrsim 1$. At the lowest temperatures, we estimate $b \simeq 4$, with a large systematic uncertainty that we characterize for later improvement. This result is consistent with Fermi liquid theory predictions for electron-electron scattering.

Acknowledgments

There are many people who contributed to this work. In particular, I would like to express my gratitude to:

Steve Dodge who is one of the most knowledgeable people that I have met and to whom it is easy to talk about anything of interest. I am most grateful to him for supporting me and giving me the opportunity to work in his lab.

Amir Farahani for teaching me how to work with the THz setup. This work could not be done without his tremendous help, guidance and support.

Payam Mousavi for sharing his exceptional programming skills, his smart ideas on how to do things and his blunt statements, but I am most grateful for his emotional and intellectual support throughout this work.

Derek Sahota for always being ready to help with anything and everything and for answering all of my questions in any area.

Ian Bushfield for his patience and guidance in the lab. He was the one who taught me the basic rules of working in the lab.

Ken Myrtle for all of his help, especially in the machine shop when I was building the mounts.

Bryan Gormann for all of his help.

Anthony Steigvilas for being so full of surprises and making our office a more interesting place.

Yongki Kim for being so kind and helpful.

Rohan Abraham for keeping the office interesting.

Ted Monchesky and Eric Karhu for providing a great MnSi sample.

Farnaz Rashidi and Shima Alagha for being my friends, my listeners, my company, and my main supports throughout this work.

Contents

Chapter 1

Introduction

Fermi liquid theory (FLT) is one of the most fundamental theories in solid state physics. It is extremely successful in describing the normal state of the majority of metals. A modified version of FLT allows us to characterize the superconducting state of many metals at low temperatures. Despite the strong Coulomb interactions between the electrons, FLT treats electrons inside metals as free particles with renormalized masses, and yet accurately predicts many properties of metals such as the specific heat, the T^2 dependence of the resistivity, and many others. The fact that the behavior of an interacting system of electrons can be very accurately predicted by considering the non-interacting system with renormalized parameters was one of the major insights gained through the success of the FLT.

Originally, FLT was developed by Landau to explain the properties of liquid He-3, but soon after it was realized that a similar approach could be used to deal with other Fermi systems, like electrons in metals. A central prediction of the theory is that currents should decay at a rate give by

$$\frac{1}{\tau(\omega, T)} = A\left[(\hbar\omega)^2 + b(\pi k_B T)^2\right], \tag{1.1}$$

where A is a material dependent constant and ω is the frequency of an applied electromagnetic field. When electron-electron scattering is the dominant source of scattering, Gurzhi showed that $b = 4$ [10]. In this thesis, we will test this prediction in the compound MnSi.

FLT is a low energy theory, and in order to investigate its predictions, like the scattering rate, one needs to be in the low frequency/temperature regime. While it was relatively simple to cool down to low enough temperatures, accessing a sufficiently low frequency range has proven to be more challenging. Quasiparticle scattering rates for many metals lie at

frequencies that remained unexplored decades after infrared and microwave spectroscopy came along. This part of the frequency spectrum was known as the "terahetz gap". Advances in ultrafast lasers in 1980s along with the development of Auston opto-electronic switches [2, 9, 25], led to the development of THz time-domain spectroscopy (THz-TDS), capable of covering the gap. One of the biggest advantages of THz-TDS is the direct measurement of the field amplitude with a subpicosecond resolution. Unlike in intensity detection methods, it is possible to extract both the real and imaginary parts of the dielectric function simultaneously. Hence, without the need for Kramers-Kronig relations, approximating extrapolations can be avoided.

MnSi is a very well-studied metal with a large variety of interesting properties. Earlier optical measurements [17] had indicated deviations from FL behavior as its scattering rate and optical conductivity did not follow FLT predictions. However, the measurements were done in the infrared frequency regime and did not extend into the THz range. This thesis extends the frequency to the THz region, and investigates the FLT predictions. In particular, this thesis is focused on testing Eq. 1.1 and finding the value of b for MnSi. Along the way, we also make several novel observations about the conductivity of MnSi, including temperature-dependent measurements of the scattering rate and plasma frequency.

This thesis is organized as follows.

- Chapter 2 is devoted to instrumentation and methods in time-domain THz spectroscopy. I explain the process of THz generation and detection using dipole antennas.
- In Chapter 3, I will discuss the process of measuring the conductivity of a thin metal film on a substrate and the models we use for analyzing the transmission amplitude data.
- In Chapter 4, I will introduce Fermi liquid theory and the quasiparticle concept, and in the end I will summarize previous studies on the relationship between the frequency-dependent resistivity and the temperature-dependent resistivity.
- In Chapter 5, I will briefly discuss the previous work on MnSi, followed by the presentation of our experimental results and conclusions.

Chapter 2

Terahertz time-domain spectroscopy

The terahertz frequency range is loosely defined as the region of the electromagnetic spectrum between 30 GHz ($\lambda = 1$ cm) to 10,000 GHz ($\lambda = 30$ μm). Spectroscopic techniques have been used to probe the infrared and microwave frequency regions for many decades, but extending these to the terahertz region proved difficult. As a result, this frequency region remained unexplored for decades, and became known as the THz gap. With the invention of the photoconductive dipole antenna in the mid 1980s [2], along with the development of ultrafast femtosecond lasers, a new era in THz technology began. This has generated intense interest in the scientific and engineering applications of terahertz radiation. Terahertz time domain spectroscopy (THz-TDS) has now found a wide range of applications, from measuring paper thickness to determining the optical conductivity of metals [7, 19]. The THz-TDS technique has numerous advantages over conventional spectroscopic techniques. Most importantly, it is a coherent technique. This enables us to obtain both the real and imaginary parts of a material's electromagnetic response function directly, without using Kramers-Kronig relations. Consequently, THz-TDS provides accurate and reliable estimates of the complex response function at terahertz frequencies [24].

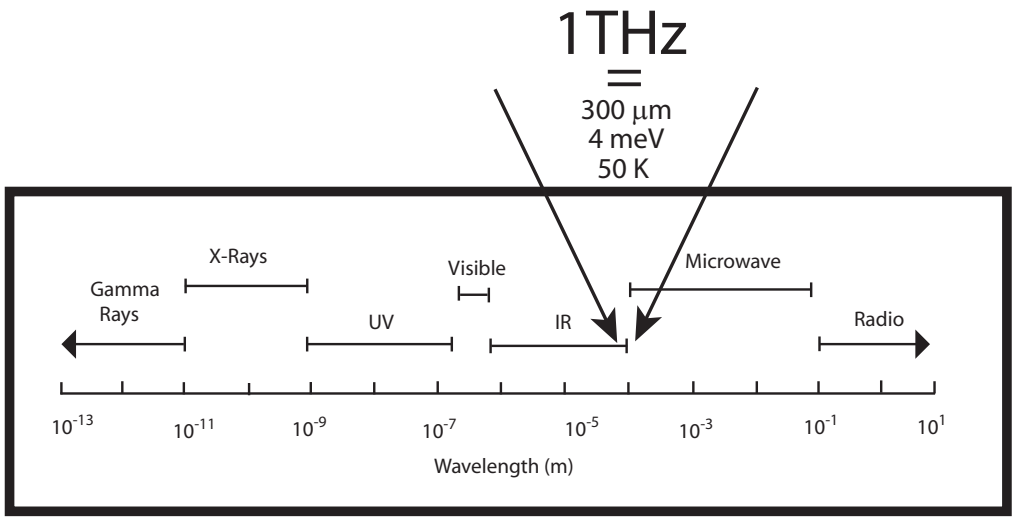

Figure 2.1: The electromagnetic spectrum with the THz gap. From Kübler [14].

2.1 Generation and detection of THz waves

In THz-TDS, there are two major methods to generate and detect THz radiation: with photoconductive antennas and with nonlinear optical techniques. We used photoconductive antennas for the work described here. In this method, terahertz pulses are generated and detected by femtosecond laser pulses incident on photoconducting dipole antennas. A remarkable symmetry in THz-TDS is that the same type of dipole antenna that generates the terahertz pulses can be used to detect them. In this case the femtosecond laser pulses serve to take time-domain snapshots of a photocurrent that gets driven by the incident terahertz pulses. In the subsequent sections I elaborate on each element in the system that we use to generate and detect THz radiation.

2.1.1 Mode-locked lasers

A laser cavity of length L has a large number of longitudinal modes that are equally spaced in the frequency domain by $\Delta\nu = c/2L$. Normally, modes have an arbitrary phase with respect to each other, which leads to a continuous flow of light in the cavity. However, if the modes have fixed phase with respect to each other (i.e. they are locked together), they interfere constructively and a series of short pulses are created in the time domain. The

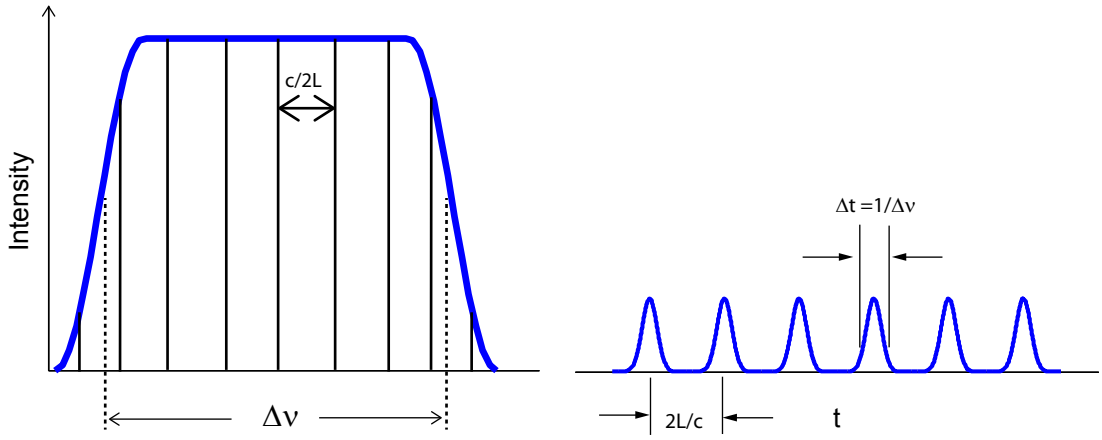

Figure 2.2: The intensity of a mode-locked laser in both the frequency domain and the temporal domain. In the frequency domain, the large number of modes is separated by c/2L with an envelope that is set by the laser medium bandwidth. In the time domain the pulse separation is 2L/c and the width of the pulse is set by the width in the frequency domain.

length of the pulse in the time domain is determined by number of modes in the frequency domain, which in turn is determined by the medium's gain bandwidth, as shown in Fig 2.2. Therefore, the length of the pulse in the time domain is inversely related to the medium bandwidth. The more modes the medium bandwidth can contain, the narrower our pulse would be in the time domain. This illustrates the need for a medium with a high gain bandwidth, for example, Ti:Sapph crystals with a bandwidth larger than 100 THz.

The laser cavity must be designed in such a way that the mode-locked state is stable with respect to the continuous state. Kerr-lens mode locking is one of the techniques to achieve this. The optical Kerr effect causes the refractive index of the crystal inside the cavity to become intensity dependent:

$$n = n_0 + n_2 I \tag{2.1}$$

where n_0 and n_2 are constants. This increases the path length of the center of beam where it has the highest intensity, just like the central ray through the convex lens. The path length difference between the central ray and rays from outside of the central region results in refraction and self-focusing of the beam. By designing the laser cavity for high efficiency

in the presence of this optically induced lens, the cavity becomes stable in the pulsed mode. In our setup we use a Ti:sapphire oscillator that in the mode-locked state generates 30 fs pulses centered at 800 nm. The repetition rate and average power are 80 MHz and 550 mW, respectively. Half of the total power is used to drive our THz-TDS setup, while the other half is directed for use in other optical systems.

2.1.2 THz generation

We generate THz pulses by directing a laser pulse at a specially engineered dipole antenna, shown schematically in Fig. 2.3. Two horizontal conducting strips serve as a parallel-wire transmission line that establishes electrical contact to the vertically oriented antenna at the center. The antenna contains a gap of a few microns that is filled with semiconductor material. To generate photocarriers across the antenna gap, the semiconductor band gap must be smaller than the photon energy of the incident beam. A bias field then accelerates the photo-induced carriers. In the far field approximation,

$$\mathbf{E}_{THz} = \frac{\mu_0}{4\pi r}[\hat{\mathbf{r}} \times (\hat{\mathbf{r}} \times \ddot{\mathbf{p}})], \tag{2.2}$$

$$\ddot{\mathbf{p}} \propto \frac{d\mathbf{j}}{dt},$$

where μ_0 is the free space permeability, r is the distance from the dipole, $\mathbf{p}$ is the dipole moment and $\mathbf{j}$ is the induced photocurrent density [8]. Consequently, the radiated THz field is proportional to the time derivative of the photocurrent, as shown in Fig. 2.4. A picosecond photocurrent pulse will then produce a nearly single-cycle pulse of broadband THz radiation.

2.1.3 THz detection

The detection process is illustrated in Fig. 2.5. As with the generation process, an ultrafast laser beam creates photocurrent across the antenna gap. Unlike the generation process, however, an incident THz pulse provides the driving field for the photocurrent. The amplitude and the direction of the photocurrent is determined by the amplitude and the sign of the THz field at the moment of photoexcitation. By monitoring the photocurrent as a function of the delay between the laser pulses at the generator and the detector, we can map the entire electric field of the pulse as a function of time.

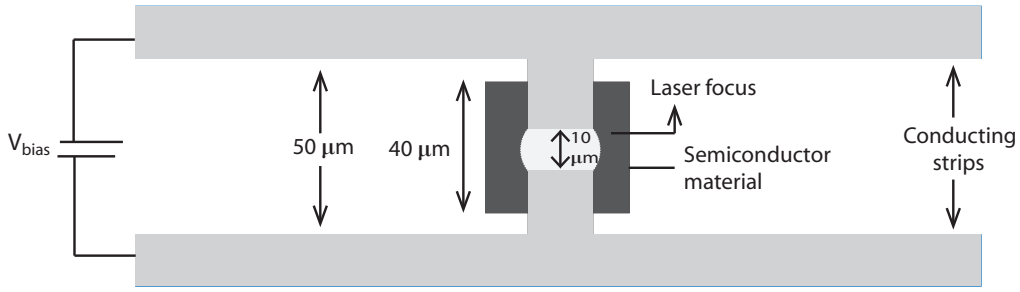

Figure 2.3: Schematic of our dipole antenna. Femtosecond laser pulses are focused on an area of semiconducting material that fills the gap between the two metal contacts, and the current flows when a bias is applied. From Lea [15].

2.1.4 Terahertz setup

The entire THz-TDS set up is shown in Fig. 2.6. The beam splitter (BS) divides the laser beam into two parts; one beam is used for generating THz pulses and the other is used for detecting them. The laser pulse excites photocarriers in the emitter antenna to generate the THz pulse. This pulse is collected and focused onto the sample via two off-axis parabolic mirrors. The pulse is transmitted through the sample located in a cryostat. Once transmitted, the pulse is collimated and focused onto the detector antenna, where it is gated by a pulse from the same laser beam that we use to generate THz pulses. The entire THz signal is mapped by varying the delay stage.

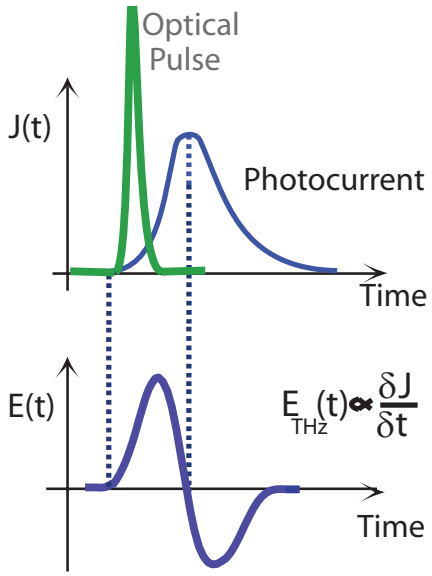

Figure 2.4: Photocurrent from antenna after being excited by an optical pulse, and the resulting THz pulse. From Farahani [6].

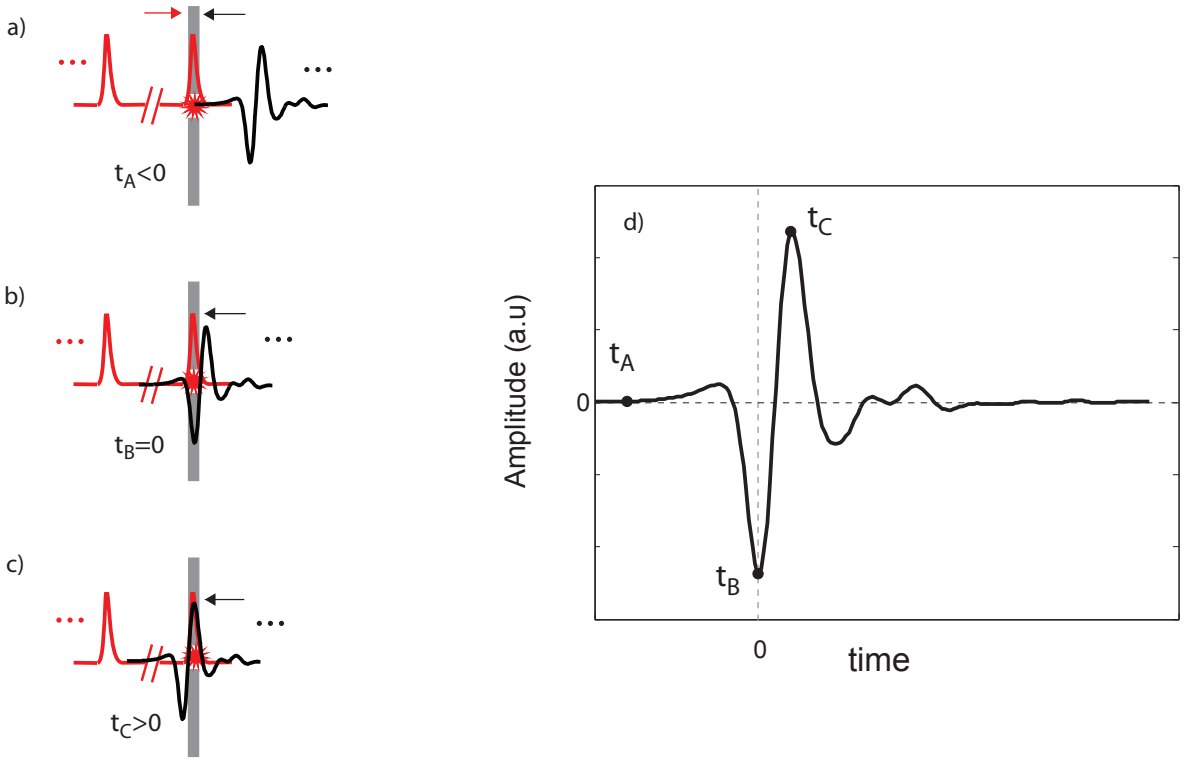

Figure 2.5: The process of THz detection. (a)The laser pulse arrives before the THz pulse and excites the photocarriers. (b), (c) The THz pulse incident on the antenna makes the current flow between two metal strips (d) The measured current maps out the THz field in time. Adapted from Dexheimer [5].

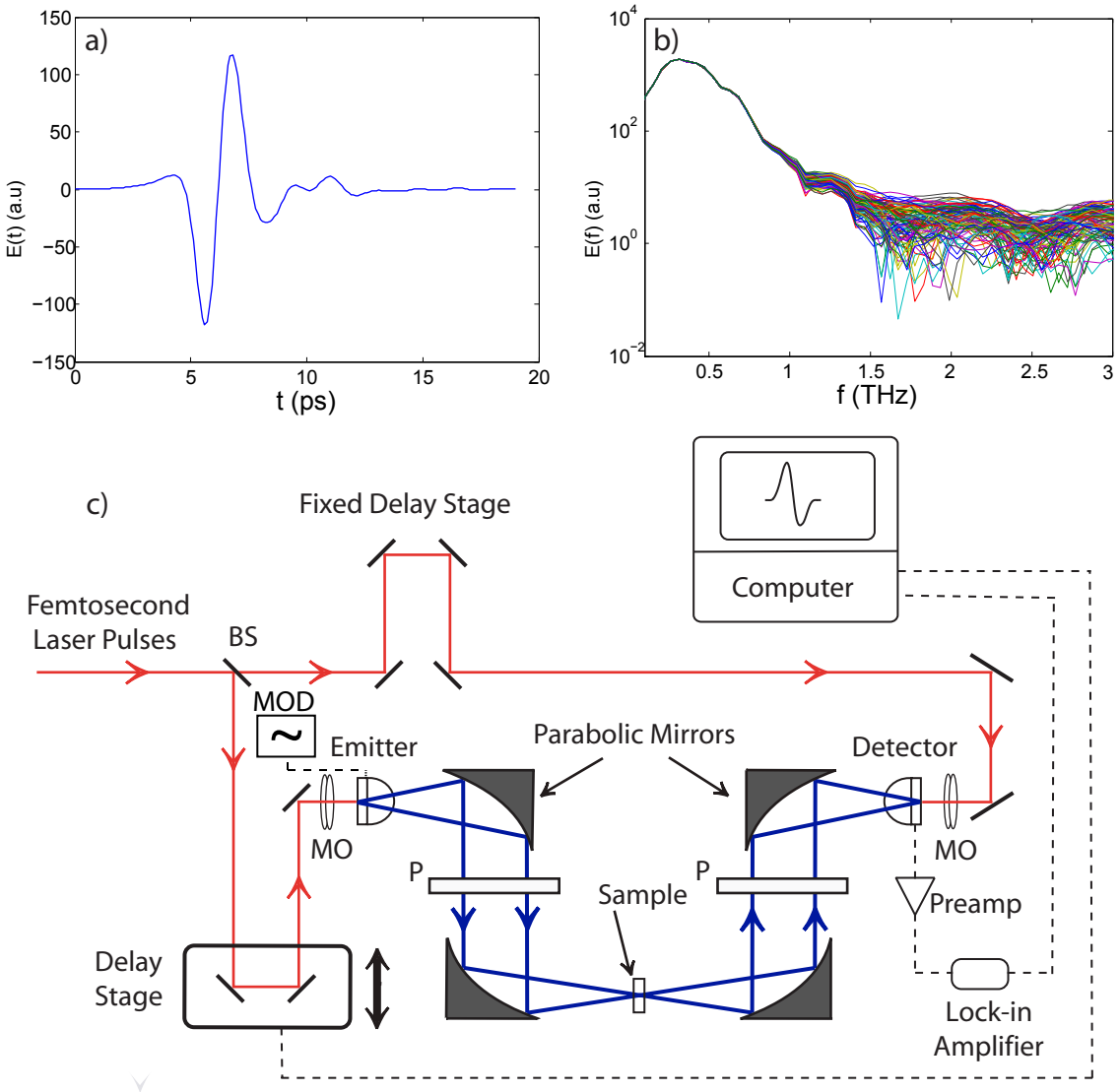

Figure 2.6: (a) Typical time-domain pulse. (b) Frequency-domain spectra of one hundred consecutive THz pulses. (c) Schematic illustration of THz-TDS setup. A beamsplitter divides the ultrafast laser beam into two arms: one goes to the detector and the other one goes to the delay stage before hitting the emitter antenna. The delay stage enables us to change the delay time between the arrival of the laser pulse and THz pulse. The emitter antenna generates a THz pulse, which is collimated then focused by two off-axis parabolic mirrors through the cryostat onto the sample. The transmitted pulse is collected and focused onto the detector antenna by two additional paraboloids. The THz pulse amplitude is modulated through the emitter bias voltage, so that the detector photocurrent can be measured with a lock-in amplifier (LIA) and recorded by the computer.

Chapter 3

Conductivity measurements with THz-TDS

We can obtain valuable information about the electronic structure of a material from the optical conductivity. In this chapter, I explain how we determine the optical conductivity from THz transmission measurements and how material properties can then be extracted from it.

3.1 Analysis methods

Our measurements are performed in transmission on a thin metallic film deposited on a transparent substrate. By comparing the field $E_{sample}(t)$ transmitted through this structure and the field $E_{ref}(t)$ transmitted through a bare substrate, we can determine the complex transmission amplitude, $\tilde{T}(\omega)$, over our measurement bandwidth. We collect our data in the time domain but we do our analysis in the frequency domain, by Fourier transforming the discrete pulses and forming the transmission quotient:

$$\begin{aligned} \tilde{E}_{sample}(\omega) &= \mathcal{F}\left\{E_{sample}\right\}, \\ \tilde{E}_{ref}(\omega) &= \mathcal{F}\left\{E_{ref}\right\} \\ \tilde{T}(\omega) &= \frac{\tilde{E}_{sample}(\omega)}{\tilde{E}_{ref}(\omega)}. \end{aligned} \tag{3.1}$$

Consideration of the boundary conditions on the electric and magnetic fields on both sides of the film leads to a relation, often known as the Tinkham formula, between the transmission

amplitude and the complex conductivity of the film:

$$\tilde{\sigma}(\omega) = \frac{n_s + 1}{Z_0 d_f}\left[\frac{1}{\tilde{T}(\omega)} - 1\right]. \tag{3.2}$$

Here n_s is the index of refraction of the substrate at terahertz frequencies, $Z_0 \simeq 377\ \Omega$ is the impedance of the free space and d_f is the film thickness [27]. Alternatively we can write the Tinkham formula in the following form:

$$T(\omega) = \frac{1}{1 + \gamma\tilde{\sigma}(\omega)}, \tag{3.3}$$

where $\gamma = dZ_0/(n+1)$. In principle, $\tilde{\sigma}(\omega)$ can take a variety of functional forms, but it is usually advantageous to assume a parameterized form like the Drude model, and then fit the resulting parameterized transfer function to the transmission amplitude. This procedure is described in the following section.

3.1.1 Transfer function fits

To obtain a sample's optical constants, we fit a transfer function $T_{2,1}(\boldsymbol{\theta};\omega)$ to the quotient $\tilde{E}_{sample}/\tilde{E}_{ref}$, where $\boldsymbol{\theta}$ is the set of fit parameters in vector form. Both $\tilde{E}_{ref}$ and $\tilde{E}_{sample}$ carry noise with variances σ_1^2 and σ_2^2 and if $\tilde{E}_{ref}$ is small, the quotient can amplify this noise. Thus, rather than minimizing the chi-squared function $\chi^2 = \sum_i \frac{1}{\sigma_i^2}|T_{1,2}(\boldsymbol{\theta};\omega_i) - \tilde{E}_{sample}(\omega_i)/\tilde{E}_{ref}(\omega_i)|$, we minimize the cost function [7]:

$$C(\boldsymbol{\theta}) = \frac{1}{2}\sum_i \frac{\tilde{E}_{sample}(\omega_i) - T_{2,1}(\boldsymbol{\theta};\omega_i)\tilde{E}_{ref}(\omega_i)}{\sigma_2^2 + |T_{2,1}(\boldsymbol{\theta};\omega_i)|^2\sigma_1^2}. \tag{3.4}$$

Rational polynomials provide a simple and common functional parameterization, where different polynomial degrees can be chosen for the numerator and denominator. Therefore, the transfer function can be represented by:

$$T_{2,1}(s) = \frac{b_0 + b_1 s + b_2 s^2 + \cdots + b_N s^N}{a_0 + a_1 s + a_2 s^2 + \cdots + a_M s^M} e^{-\eta s}. \tag{3.5}$$

Here $s = i\omega$ and we include $e^{-\eta s}$ to account for the delay associated with any optical thickness mismatch between the reference and sample substrates. As written, all of the parameters $\{a_n\}$ and $\{b_n\}$ may be rescaled by constants without changing the function $\tilde{T}(\omega)$, so we must fix the scale by setting one of the parameters to a constant, for example $a_0 = 1$. We refer to a transfer function with polynomials of degree M and N as an (M, N) model. In this work we use (0,0), (1,1), and (2,2) models, as described below.

3.1.2 Drude parameter estimation

Extracting parameters from our data can now be done in two steps:

I. Finding the thickness mismatch between substrates

Typically, the optical thicknesses of our reference and sample substrates are measurably different. The thickness mismatch introduces a phase shift in our transmition amplitude,

$$\tilde{T}(\omega) = \exp\left[\frac{i\omega n_s}{c}(d_2 - d_1)\right], \tag{3.6}$$

that must be considered in the analysis. To find the mismatch, we fit a (0,0) model with a delay η to the transmission amplitude ratio:

$$\tilde{T}(\omega) = \frac{\tilde{E}_{sample}(\omega)}{\tilde{E}_{ref}(\omega)} = b_0 e^{-\eta s}. \tag{3.7}$$

This gives

$$\eta = \frac{n_s}{c}(d_1 - d_2). \tag{3.8}$$

Ideally, after characterizing this mismatch in a set of substrates, a thin metallic film is deposited on the sample substrate for comparison with a known reference.

II. Extract parameters from Drude conductivity model

Using the assumption that free electrons undergo diffusive motion with an average scattering lifetime τ, Drude derived an equation for the conductivity in metals:

$$\sigma(\omega) = \frac{\sigma_0}{1 - i\omega\tau},\ \sigma_0 = \frac{ne^2\tau}{m} = \epsilon_0\omega_p^2\tau, \tag{3.9}$$

where n is the carrier density, m is the carrier mass, ϵ_0 is the free space permittivity, τ is the scattering lifetime, and $\omega_p = \sqrt{ne^2/\epsilon_0 m}$ is known as the plasma frequency. After shifting the reference pulse to account for the substrate thickness mismatch, Eq. 3.3 then yields a (1,1) rational polynomial model for the transfer function,

$$T(s) = \frac{-1/\tau + s}{-(1/\tau + \gamma\epsilon_0\omega_p^2) + s} = \frac{b_0 + b_1 s}{a_0 + a_1 s}, \tag{3.10}$$

with $b_1 = a_1 = 1$, and

$$\tau = -\frac{1}{b_0}, \quad \epsilon_0\omega_p^2 = \frac{b_0 - a_0}{\gamma}. \tag{3.11}$$

The product of τ and $\epsilon_0\omega_p^2$ gives the dc conductivity,

$$\sigma_0 = \frac{1}{\rho} = \epsilon_0\omega_p^2\tau. \tag{3.12}$$

Experimentally, both τ and ρ have relatively constant uncertainties, so we focus on

$$\omega_p^{-2} = \epsilon_0\rho\tau \tag{3.13}$$

to avoid the divergent uncertainty in $b_0 = -1/\tau$ as τ approaches zero.

3.1.3 Fermi liquid parameter estimation

Fermi liquid theory predicts that at low frequencies and temperatures the conductivity of a metal should approach the Drude model, with a correction due to electron-electron scattering:

$$\sigma(\omega) = \frac{\epsilon_0\omega_p^2}{1/\tau - i\omega + B\omega^2}. \tag{3.14}$$

Together with Eq. 3.3, this gives a (2,2) rational polynomial model for the transfer function,

$$T(s) = \frac{-1/\tau + s - Bs^2}{-(1/\tau + \gamma\epsilon_0\omega_p^2) + s - Bs^2} = \frac{b_0 + b_1 s + b_2 s^2}{a_0 + a_1 s + a_2 s^2}, \tag{3.15}$$

with $b_1 = a_1 = 1$, $\tau = -1/b_0$, and $\epsilon_0\omega_p^2 = (b_0 - a_0)/\gamma$ as in the Drude model, and a Fermi liquid scattering amplitude given by

$$B = -a_2 = -b_2. \tag{3.16}$$

3.2 Analysis

3.2.1 Substrate matching

The substrate mismatch is measured prior to the film deposition. After characterizing two substrates from the same batch, one is kept as the reference and the other one is sent for the film deposition. The optical thickness mismatch of the substrates used in our experiment is small and independent of temperature, so it is sufficient for us to make repeated measurements of η at room temperature and fit the results with a (0,0) model to get an overall value for η. Fig. 3.1 shows a typical distribution of 100 η measurements. In a typical experiment, we can obtain an uncertainty of $\sigma_{\bar{\eta}} \simeq \sigma_\eta/\sqrt{N} \simeq \pm 0.2$ fs. In the experiments discussed in this thesis, the absolute mismatch between the sample and reference substrates is always less than 10 fs.

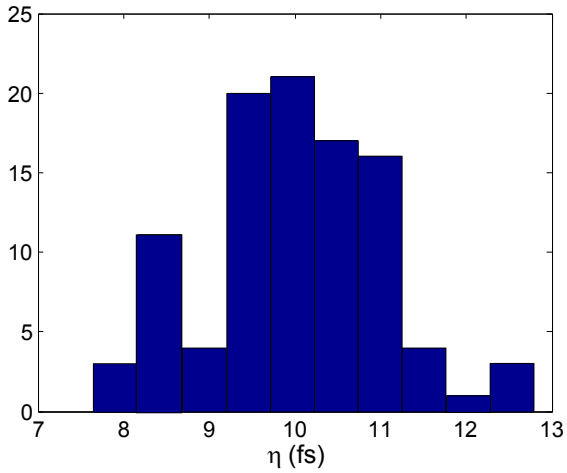

Figure 3.1: The distribution of 100 repeated measurements of η at room temperature.

3.2.2 Analysis example

To illustrate the analysis method, Fig. 3.2 shows the reference and sample pulses for a thin film of MnSi at T=40 K.

The lower part of the figure shows the time-domain fit residuals, defined as

$$R(t) = E_{sample}(t) - \mathcal{F}^{-1}\left\{\tilde{T}(\boldsymbol{\theta};\omega)E_{ref}(\omega)\right\}, \tag{3.17}$$

where $\boldsymbol{\theta}$ is a vector of the fit parameters, $\boldsymbol{\theta} = [\omega_p^2, \tau]$. Although the residuals show clear structure indicative of systematic errors in the measurement, the magnitude of the residuals is two orders of magnitude smaller than the signal amplitude. From repeated measurements on the same sample we can estimate the resulting uncertainty in τ to be less than a few femtoseconds.

The inset of Fig. 3.2 shows that the sample pulse appears to arrive ahead of the reference pulse. A naive interpretation of this is that the THz pulse propagates through the MnSi film faster than the speed of light, but it is more correct to describe this phenomenon as pulse distortion. For high sheet conductivity, $\tilde{\sigma}(\omega)d$, the transmission amplitude is small, $|\tilde{T}| \ll 1$, and can be written as:

$$\tilde{T}(\omega) \propto \frac{1}{\tilde{\sigma}(\omega)} \simeq \frac{1 - i\omega\tau}{\sigma_0} \simeq \rho_0 e^{-i\omega\tau}. \tag{3.18}$$

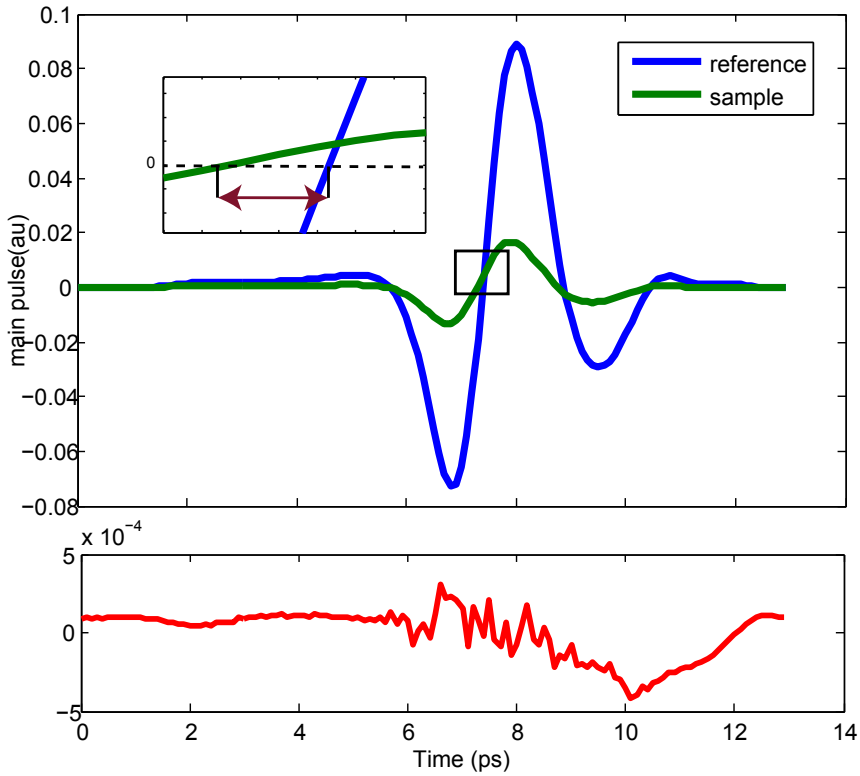

Figure 3.2: The sample and reference pulse at T=40 K. The inset shows the zero crossings of the sample pulse and the reference pulse. The time difference between these two is approximately the scattering lifetime. The bottom of the figure shows the residual which is smaller than the pulse by two orders of magnitude.

Considering the reference pulse as a harmonic plane wave $E_{ref} = E_0 e^{-i\omega t}$, the sample pulse can be written as $E_s = E_0 \rho_0 e^{-i\omega(t+\tau)}$. The sign of this phase shift produces a negative delay that is directly related to the scattering lifetime. The arrow shows the difference in zero crossing of two pulses which approximately is equal to the scattering lifetime.

3.2.3 Procedure at low temperatures

For low temperature measurements, our samples are mounted on a sample holder that moves vertically in a cryostat that has a continuous flow of liquid He. The terahertz pulses enter and exit horizontally through two cryostat windows. The samples are mounted on apertures as shown in Fig. 3.3. In our setup a set of three circular apertures is used. We make transmission measurements through the bottom, middle and top apertures consecutively, and then change the temperature for next set of measurements. At low temperatures, the measurements of η develop a dependence on the cryostat temperature that we must remove. Previous measurements in our lab by Saeid Kamal and Graham Lea showed that the optical path length of the cryostat windows changes as $\eta(T) = C/T$, where C=2570 fs-K and T is the temperature inside the cryostat. Our working hypothesis is that moving the sample holder up and down causes a slight temperature fluctuation inside the cryostat that leads to a change in the optical path length of the windows. To reduce this systematic error, we mount the sample between the two references as Fig. 3.3 shows. Taking the average of transmission pulses between top and the bottom substrate cancels this error to the first order [15].

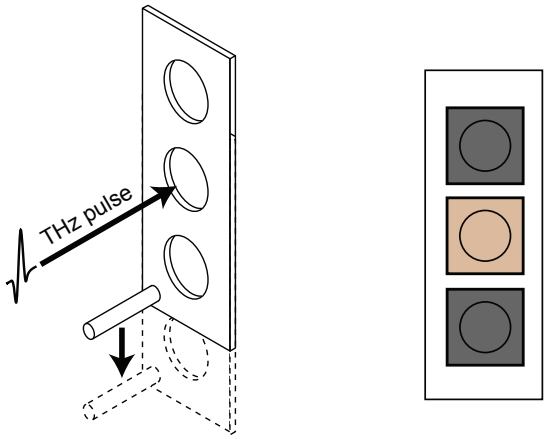

Figure 3.3: Sample positioning and mounting. Left: Our apertures move vertically as we take measurements on different specimens. Right: typical sample mounting arrangement, with our sample of interest typically placed between the two references. From Lea [15].

Chapter 4

Experimental consequences of Fermi liquid theory

4.1 Introduction

Fermi liquid theory (FLT) was developed by Lev Landau to explain the properties of liquid He-3, but it successfully captures the physics of a wide range of degenerate interacting Fermi systems, from neutron stars to conventional metals. Today, it is commonly referred to as the Standard Model of the metallic state, to emphasize its fundamental nature. Fermi liquid theory explains why a strongly interacting system of fermions behaves like a non-interacting system in many respects. The basic idea is to incorporate interactions in a phenomenological way that I will explain in this chapter.

A central prediction of Fermi liquid theory is that the conductivity of a metal should depend quadratically on both temperature and frequency,

$$Re(\sigma^{-1}(\omega, T)) - \rho_0 \propto 1/\tau = A[(\hbar\omega)^2 + b(\pi k_B T)^2] \tag{4.1}$$

where ρ_0 is the residual resistivity, A is a constant that varies with material, and b is a constant, equal to four in FLT, that we will call the frequency-temperature (ω-T) scaling parameter [10]. Although b has been determined for many materials, none of them has agreed with the FLT prediction of $b = 4$. As I will show in Ch. 5, we have obtained preliminary evidence that the THz conductivity of MnSi agrees with Eq. 4.1 with $b \to 4$ as $T \to 0$, in agreement with FLT. Before presenting these results, in this chapter I will review the origin of Eq. 4.1 and previous measurements of the scaling factor b.

4.2 Fermi liquid theory

4.2.1 Historical background

In an attempt to construct models to describe the qualitative and quantitative properties of metals, physicists came up with the noninteracting electron gas model. The assumption was that when atoms of a metallic element are brought together to form a metal, the valence electrons become detached and electrons move freely while ions remain immobile. Drude assumed that the electrons form an ideal gas with a Boltzmann velocity distribution. This yielded good agreement with the resistivity values at room temperature and with the Wiedemann-Franz law of thermal conductivity, but also predicted a value of $3nk_B/2$ for the specific heat that was much larger than the experimentally observed values for typical metals [1]. This puzzling situation was resolved when the Pauli exclusion principle was introduced and Sommerfeld replaced the Maxwell-Boltzmann distribution by the Fermi-Dirac distribution. The Sommerfeld theory of metals, which adapts the classical Drude model to the case of quantum Fermi-Dirac statistics, correctly predicts the Wiedemann-Franz law, explains both the conductivity and specific heat of metals, and provides a framework for understanding a wide range of other phenomena in metals [1]. The success of the Sommerfeld theory created another puzzle, however: it ignores electron-electron interactions, which are known to be strong at metallic densities. Landau's Fermi liquid theory explained how this occurs.

Studies of liquid He-3 showed that its behavior is strongly influenced by quantum effects, and due to these effects, He-3 is liquid at T=0 K and the ambient pressure. Landau theory is the first theory of quantum liquids that describes the properties of a so called Fermi-liquid system. This type of quantum system consists of interacting particles with spin 1/2 that obey Fermi-Dirac statistics. This class of material includes liquid He-3, electrons in metals and heavy nuclei. The building block of the Fermi liquid theory (FLT) is quasiparticles, which I will review it in the following section.

4.2.2 Quasiparticles

Landau imagined a dense system in which interactions between particles increases gradually from zero to some maximum value given by experiment. If the turning on procedure is slow enough, the eigenstates of the noninteracting system will transform into eigenstates of the

interacting system smoothly, with a rigorous one-to-one correspondence. For each particle in the non-interacting system, there is a "quasiparticle" in the interacting system with the same momentum, spin and charge. Similar to particles in the non-interacting system, quasiparticles obey the Pauli exclusion principle. However, the Fermi velocity and effective mass are renormalized from their noninteracting values. In Landau's picture, the particle moves with the distortion brought by the interaction, and it is dressed with a self-energy cloud. The dressed particle is known as a quasiparticle with the effective mass m^*.

Like a noninteracting Fermi gas, the ground state of quasiparticles is filled up to the Fermi momentum $p_F = \hbar k_F$, and an excited state is created by putting a quasiparticle in an unoccupied state is denoted by $(\boldsymbol{p}, \sigma)$. The energy of the quasiparticle is given by the usual expression, with an effective mass m^*:

$$\epsilon(p) = \frac{p^2}{2m^*}, \tag{4.2}$$

Similarly, the Fermi velocity and density of states for a spherical Fermi surface are given by:

$$v_F = \frac{p_F}{m^*}, \tag{4.3}$$

$$\frac{dN}{d\epsilon} = \frac{3Nm^*}{p_F^2}, \tag{4.4}$$

and the specific heat is

$$c_v = \frac{m^*(3\pi^2 N)^{1/3}}{3\hbar^2} k_B^2 T. \tag{4.5}$$

4.3 Quasiparticle decay rate

If a quasiparticle above the Fermi surface undergoes a collision with another quasiparticle below the Fermi surface, the dominant scattering process is to create a quasiparticle-quasihole pair. This process is shown schematically in Fig. 4.1, in which a quasiparticle with momentum $\mathbf{p_1}$ scatters into a state with one quasihole at $\mathbf{p_2}$ and two quasiparticles at $\mathbf{p_3}$ and $\mathbf{p_4}$:

$$\mathbf{p_1} + \mathbf{p_2} \rightarrow \mathbf{p_3} + \mathbf{p_4}. \tag{4.6}$$

The constraints on the magnitude of the particles are $|\mathbf{p_2}| < p_F$, $|\mathbf{p_3}| > p_F$ and $|\mathbf{p_4}| = |\mathbf{p_1} + \mathbf{p_2} - \mathbf{p_3}| > p_F$. For $|\mathbf{p_1}| - p_F \ll p_F$,

$$2p_F - |\mathbf{p_1}| < |\mathbf{p_2}| < p_F \tag{4.7}$$

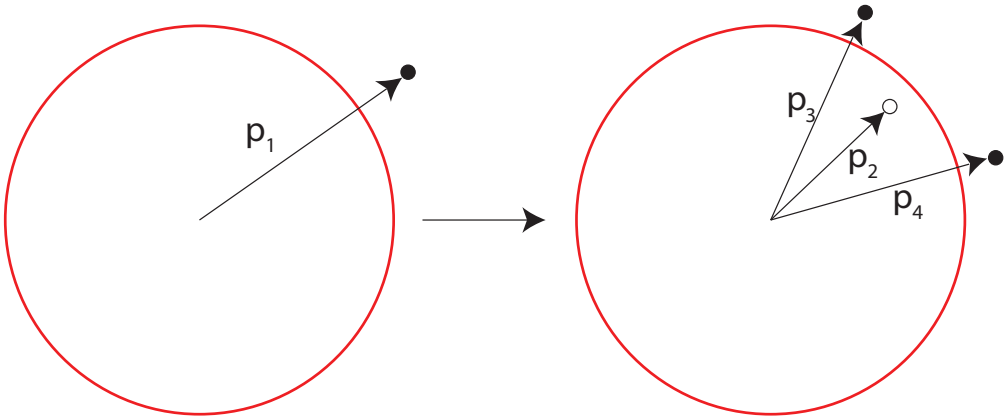

Figure 4.1: The kinematics of the decay of quasiparticles near the Fermi surface (From lecture notes by D. Broun).

$$p_F < |\mathbf{p_3}| < |\mathbf{p_1}| + |\mathbf{p_2}| - p_F. \tag{4.8}$$

By Fermi's golden rule, the total probability of Eq. 4.6 is proportional to the density of final states,

$$\rho(p_2, p_3) = \int \delta(\epsilon_1 + \epsilon_2 - \epsilon_3 - \epsilon_4) d\mathbf{p_2} d\mathbf{p_3}. \tag{4.9}$$

For fixed ϵ, this becomes:

$$\int_{2p_F - p_1}^{p_F} dp_2 \int_{p_F}^{p_1 + p_2 - p_F} dp_3 = \frac{1}{2}(p_1 - p_F)^2 \tag{4.10}$$

$$\propto (\epsilon_1 - \epsilon_F)^2. \tag{4.11}$$

At low temperatures, T plays the role of energy, causing the Fermi-Dirac distribution to develop a width of $k_B T$ in energy. This leads to an increase of the density of final states by $(k_B T)^2$ and consequently to an increase of the decay rate:

$$\frac{1}{\tau_{qp}} = a[\epsilon^2 + (\pi k_B T)^2]. \tag{4.12}$$

Here, τ is the decay rate of a single quasiparticle, and π accounts for the first Matsubara frequency in the complex plain. To understand conductivity, however, we must consider the lifetime of two-particle states, since a quasiparticle must make a transition from one state into another to produce a current. Accounting for this, we get a relationship for the

frequency and temperature dependent resistivity that is qualitatively similar to the single-particle scattering rate,

$$\frac{1}{\tau_{opt}} = Re[\rho(\omega, T)] = A[(\hbar\omega)^2 + b(\pi k_B T)^2],$$

but with $b = 4$, not $b = 1$. The origin of this difference comes from the single-particle and two-particle excitations. The single-particle excitations are fermions, while the two-particle excitations are bosons. Green's function has different responses in each case that makes $b = 1$ or 4. $b = 4$ in the two particle scattering was worked out by Gurzhi for the first time and has been revisited ever since [10, 16]. Recently, it reemerged as a topic of interest, and Maslov and Chubukov [16] showed that the magnitude of b depends on the interplay between inelastic (electron-electron) and elastic scattering. If the scattering is purely inelastic $b = 4$, in the case of purely elastic scattering $b = 1$, and if the source of scattering is a mixture of elastic and inelastic, $1 < b < \infty$. Experimentally, the value $b = 4$ expected from FLT has never been observed. One of the experimental challenges has been to access the regime in which FLT is valid, with $\hbar\omega \sim k_B T$ at relatively low temperatures. Recognizing the significance of this region, this thesis investigates the properties of a FLT metal in the terahertz region, where $\hbar\omega$ is comparable to $k_B T$ at low temperatures. We measured the dynamical conductivity of MnSi in THz region, and find that $b \simeq 4$ at low temperatures. Before presenting the results of our measurements, I will review other works related to measurements of b.

4.4 Previous measurements of the ω-T scaling parameter

4.4.1 Temperature range of FLT

Before discussing specific experiments, I would like to start by looking more closely on the temperature range that FLT is valid. FLT is a low energy theory, restricted to a particular frequency and temperature range. More recently, Berthod *et al.* [4], Maslov and Chubukov [16] extended the range into a higher temperature regime where resistivity no longer behaves like ω^2 and T^2. However, one still needs to be in a particular temperature range to test FLT. Berthod *et al.* [4] showed that FLT applies fully below $T_{FL} \simeq 0.1T_0$, and breaks down completely at $T_1 = 3T_0/8$, where T_0 can be obtained from the following relation:

$$\frac{\hbar}{\tau(\omega)} = \frac{2}{3\pi k_B T_0}[(\hbar\omega)^2 + (2\pi k_B T)^2]. \tag{4.13}$$

We must be well below T_0 to obtain a conclusive result regarding the FL behavior. We can experimentally determine T_0 by finding the coefficient A, where $\rho(T) = \rho_0 + AT^2$,

$$AT^2 = \frac{1}{\epsilon_0 \omega_p^{*2} \tau^*(0)} = \frac{1}{\epsilon_0 \hbar \omega_p^{*2}} \frac{2}{3\pi k_B T_0} (2\pi k_B T)^2 \tag{4.14}$$

where $\omega_p^{*2} = \omega_p^2/(1+\lambda)$ is the square of the *renormalized* plasma frequency, determined from an optical measurement. By comparing Eq. 4.13 and Eq. 4.14 we find

$$T_0 = \frac{8\pi k_B}{3\epsilon_0 \hbar} \frac{1}{A\omega_p^{*2}} \simeq \frac{1.24 \times 10^{23}}{A\omega_p^{*2}} \text{ [K]}, \tag{4.15}$$

where A and ω_p^{*2} are determined experimentally, with units of Ω-m/K^2 and s^{-2}, respectively. Using this method, I calculated T_0 for the following works and comment on whether they are in the right temperature regime or not. Table 4.4.1 shows the results of these calculations.

Material	UPt_3	Hg1201	$Ce_{.95}Ca_{.05}TiO_{3.04}$	$Nd_{1-x}TiO_3$	URu_2Si_2	MnSi
T_0 (K)	17	719	1156	1037	103	180

Table 4.1: The summary of T_0 estimations for different materials discussed in this chapter.

4.4.2 Absorptivity of UPt_3

Sulewski *et al.* [26] measured the absorptivity of UPt_3 for $\lambda = 50 - 1000$ cm^{-1} from T=1.2-300 K. By relating the absorptivity to the resistivity, they determined the magnitude of b in the far infrared region. To cover the wide frequency range of the measurements, they used two different methods to generate the radiation and three techniques to determine the absorptivity. From 50 to 1000 cm^{-1}, they used a Michelson interferometer with a mercury arc, and from 2 to 60 cm^{-1}, they used a lamellar grating interferometer in place of the Michelson interferometer. To measure the absorptivity, from 2 to 30 cm^{-1}, the transmission line technique was used; from 10 to 300 cm^{-1}, the nonresonant cavity technique was used; and from 250 to 1000 cm^{-1}, the absorptivity was obtained after the incident light makes two reflections from the UPt_3 sample at 45 degree angle of incidence. Since we are interested in the measurement in the frequency region $\lambda < 60$ cm^{-1}, I focus on the transmission line technique.

In the region $\lambda < 30$ cm^{-1} and $T = 1.2 - 55.6$ K, since the absorptivity is small, they used a transmission-line technique with large sensitivity. This apparatus consists of two coaxial cables with a rod of polycrystalline UPt_3 serving as the center conductor for one

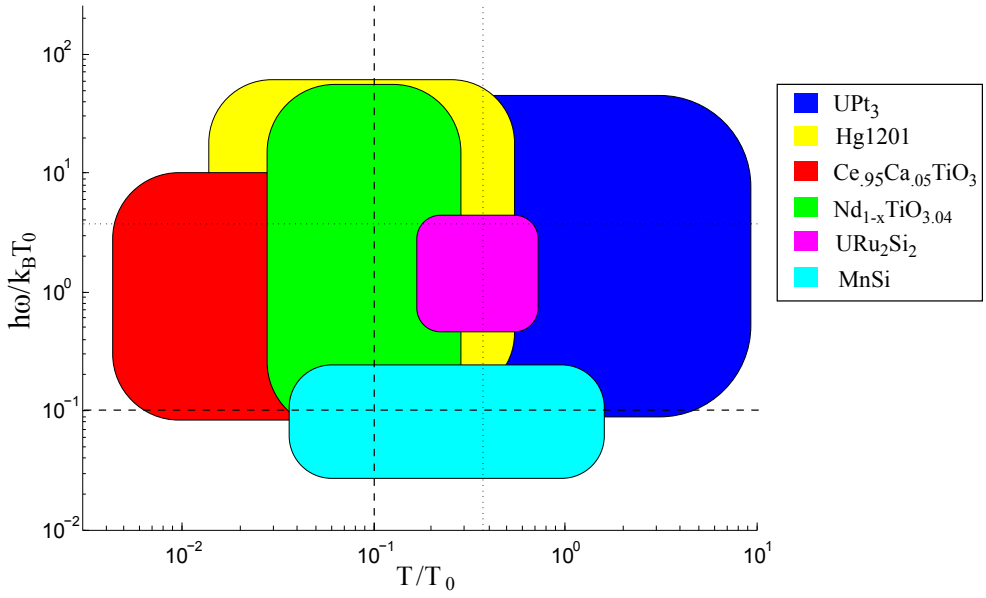

Figure 4.2: The frequency and temperature range that is covered for each material discussed in this chapter. Each material is denoted by a different colored rectangle that extends over the frequency and temperature range of the measurement. The dotted line at $T_1/T_0 = 3/8$ corresponds to the coherent regime in which the FLT is broadly valid and the dashed line at $T_{FL}/T_0 = 0.1$ corresponds to where FLT applies fully. The analogous frequencies are also indicated [4].

of them and a copper rod as the center of the other one, to serve as a reference. Both the UPt_3 sample and the copper reference cables have copper outer conductors. To measure the absorptivity, the ratio of the transmission of the two coaxial cable were compared and absorptivity of UPt_3 was determined. After the measurement process, they obtained the complex conductivity by performing a Kramers-Kronig transformation. The data shows that dc resistivity has a T^2 dependence at temperatures below 2 K, and the scattering rate has the form expected from FLT,

$$\frac{1}{\tau} \sim (k_B\omega)^2 + (b\pi k_B T)^2, \tag{4.16}$$

but with $b \leq 1$, in quantitative disagreement with FLT. Fig. 4.2 shows the frequency and temperature range that they covered. According to the T_0 value for this material, they covered a low energy and temperature range, and test the FLT in the proper range. Therefore, b is indeed in disagreement with the FLT prediction for UPt_3.

4.4.3 Infrared reflectivity of $HgBa_2CuO_{4+\delta}$

Mirzaei *et al.* [18] measured the infrared reflectivity of the compound $HgBa_2CuO_{4+\delta}$ (Hg1201) for energy range 8 meV to 3.7 eV from $T = 10 - 390$ K. A Fourier transform spectrometer was used to measure the energy range from 8 meV to 1.24 eV and the ellipsometry technique was used to measure the energy range $0.8 - 3.7$ eV. Mirzaei *et al.* found that the resistivity is proportional to T^2 for the range of $T = 70 - 223$ K and the scattering rate follows the universal form $(\hbar\omega)^2 + (b\pi k_B T)^2$, with $b \simeq 1.5$. Fig. 4.2 shows the frequency and temperature range that Mirzaei *et al.* did their measurements, in the unit of T_0. Although the temperature range is in the optimum region $T<.1T_0$ to investigate the FL behaviors, the energy range is higher than the optimum frequency region. So, the value of b might be different at lower frequencies where FLT applies fully, but it crosses over to 1.5 for energy range higher than 8 meV.

4.4.4 Optical conductivity of $Ce_{.95}Ca_{.05}TiO_{3.04}$

Katsufuji *et al.* [13] studied the optical conductivity of $Ce_{.95}Ca_{.05}TiO_{3.04}$ for the energy range of .01-3 eV and temperature range of T=5-290 K. They measured the reflectivity from a single crystal of $Ce_{.95}Ca_{.05}TiO_{3.04}$ and by using Kramers-Kronig transformation, they inferred the optical conductivity. For a wide energy range (from .01-1 eV) the scattering

rate $\hbar/\tau$ is proportional to T^2 and they claim that the scattering rate follows Eq. 4.1 with $b = 1.7$. This conclusion was based on the data presented in Fig. 4.3. Part (a) of this figure

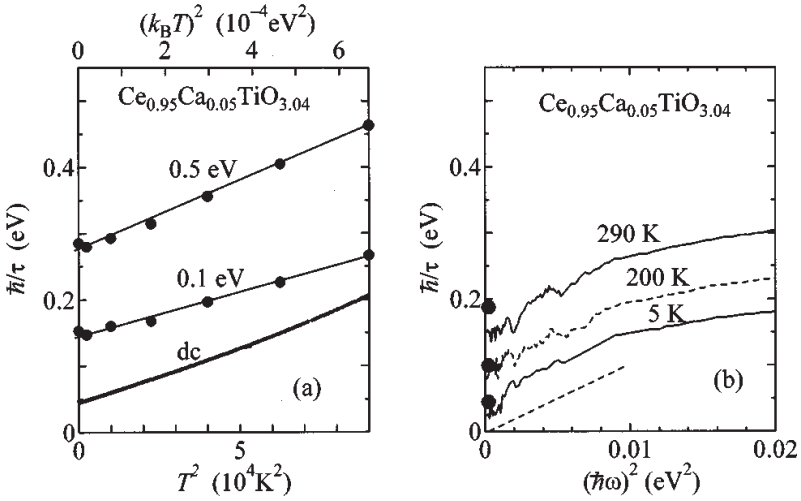

Figure 4.3: (a) The scattering rate ($\hbar/\tau$) as a function of T^2 at different frequencies. (b) The scattering rate ($\hbar/\tau$) as a function of $(\hbar\omega)^2$ at various temperatures. Closed circles show the dc value of the same sample. The slope of the dashed line represents the estimated ω^2 coefficient in the scattering rate in Eq. 4.17. From Katsufuji *et al.* [13].

is the scattering rate as a function of T^2 for different energies. Part (b) is the scattering rate as a function of $(\hbar\omega)^2$ at various temperatures. They argue that the scattering rate has a linear relationship with $(\hbar\omega)^2$ and the slope for all temperatures are identical for $(\hbar\omega)^2 < .01$, equal to 12 eV^{-1}. By using the following relation:

$$\frac{\hbar}{\tau} = \frac{\hbar}{\tau_0} + \alpha(k_BT)^2 + \beta(\hbar\omega)^2, \tag{4.17}$$

and information from Fig. 4.3, they find the magnitude α/β to be 17 which makes $b = 17/\pi^2 \simeq 1.7$, which they assert is consistent with b$\simeq$1. Throughout this paper, authors mistakenly assume that FLT predicts $b = 1$, and argue that their result is consistent with the theory.

Using Eq. 4.13 and information from Fig 4.3, I found T_0=108 K. Their measurements include only one spectrum at $T \ll 108$ K, however. Due to the poor signal to noise at low frequencies, the slope of the curve is not very well defined. The poor signal to noise can be observed in the inconsistency of their optical measurements and the dc measurements,

where none of the closed circles matches with the value of the optical conductivity at $\omega = 0$, Fig. 4.3(b). As Fig. 4.2 suggests, for the most part they are in a range with temperature higher than T_0, and only one measurement was done in low enough temperature. So, the value of b determined only at one temperature and at the region that the signal to noise ratio is poor can not be considered a reliable test of FLT [13].

4.4.5 Optical spectroscopy of $Nd_{1-x}TiO_3$

Yang *et al.* [29] used a Fourier transform spectrometer to measure the optical conductivity of $Nd_{1-x}TiO_3$ between 50 and 40000 cm^{-1} for different doping levels at six different temperatures ranging from 28 K to 295 K. They measured the normal-incident reflectance from a single crystal of the sample located in a helium flow cryostat and obtained the conductivity information by Kramers-Kronig analysis. The scattering rate was obtained by fitting the conductivity at different temperatures to the extended Drude model,

$$\sigma(\omega, T) = \frac{1}{4\pi} \frac{\omega_p^2}{1/\tau(\omega, T) - i\omega[1 + \lambda(\omega, T)]}, \tag{4.18}$$

where $\sigma(\omega, T)$ is the complex optical conductivity, ω_p is the plasma frequency, $1/\tau$ is the scattering rate, and $1+\lambda(\omega) = m^*(\omega)/m$ is the mass renormalization. Yang *et al.* find that for $x = .095$, the sample becomes metallic and displays Fermi-liquid behavior at low frequencies. They show that the scattering rate follows Eq. 4.1 with $b = 1.1$. The authors in this paper also assert incorrectly that FLT predicts $b = 1$, and according to this assumption they argue that their result is consistent with the theory. This claim is based on the data presented in Fig. 4.4. In Fig. 4.4(a), they plot the scattering rate spectra at various temperatures as a function of frequency squared. They assert that the curves are linear and parallel to each other, but note that the dependence on ω^2 deviates from the linear shape at lower temperatures. The solid line in Fig. 4.4(a) is the least square fit to the room temperature scattering rate. The dashed line is the slope that gives $b = 4$, which I plot for comparison. Fig. 4.4(b) shows the scattering rate as a function of $(k_B T)^2$. The solid triangles represent the scattering rate derived from four point probe resistivity measurements, and the dashed line is the linear fit to the points. The closed circles are the dc resistivity obtained by optical measurements and the dashed line is the linear fit to it. The slopes of the two linear fits are different, and authors used the slope of the optical measurement to find b. By using the information from the dc resistivity fit and the slope of the linear fit to the room temperature data in Fig. 4.4(a), they determine the magnitude of b in Eq. 4.1 to be 1.1.

Using Eq. 4.13 and information from Fig 4.4(b), I found two values of T_0, one based on the direct dc resistivity measurement and one based on the optical measurement. For the direct dc measurement, T_0=344 K and for the optical measurement, T_0=1036 K.[1] So, the temperature range to investigate FLT properties is $T < 86$ K or $T < 259$ K. Since the authors used the slope of the optical measurements to find b, I used T_0 that is obtained from optical measurements to plot Fig. 4.2. $T_0 = 259$ K, puts most of their measurements in the right temperature range. However, to find b they used the slope of the room temperature measurements, which would give a value of T_0 that would put them outside of the proper temperature range. The other issue here is their poor signal to noise ratio at the low frequency range where they did their investigations. This can be observed in Fig. 4.4(b), where the slope of the direct dc measurements and the optical measurements are so different. This discrepancy, together with the poor signal-to-noise ratio of the data used in their fits, raises questions about the value of b that they obtained and the degree to which it can be considered a reliable test of FLT.

4.4.6 Optical spectroscopy of URu_2Si_2

Nagel *et al.* [20] used infrared spectroscopy to measure the reflectance of a single crystal of URu_2Si_2 for the temperature range 5 K to 75 K. They obtained the optical conductivity by using Kramers-Kronig analysis and argue that the frequency-dependent resistivity of URu_2Si_2 follows Eq. 4.1 with $b = 1$. This conclusion is based on the data presented in Fig. 4.5. Part A of this plot shows the scattering rate as a function of frequency for three different temperatures and the dashed line is $1/\tau^* = \omega$. The significance of this line is that FLT applies where $1/\tau < \omega$, so only $T = 20$ K is in the FLT regime while other are not [4]. The scattering rate was acquired by applying the extended Drude model, Eq. 4.18, to the conductivity. Part B of Fig. 4.5 shows the resistivity as a function of frequency for three different temperatures, where solid circles represent the dc resistivity, measured separately. The dashed lines are fits to $\rho(\omega) = A'\omega^2 + c$, with $A'(T)$ and $c(T)$ as fit parameters. By comparing this equation with

$$\rho(\omega) = A[(\hbar\omega)^2 + b(\pi k_B T)^2],$$

[1] Since Yang *et al.* does not indicate the value of the mass renormalization, m^*/m assumed to be 4.

we find that $c(T) = Ab(\pi k_B T)^2$. The inset of Fig. 4.5(B) is $c(T)$ as a function of T^2. Therefore, the slope gives the coefficient $A' = b(\pi)^2 A = .3\,\mu\Omega$-cm K^{-2}, which results in $b = 1$. This conclusion is based on a least-squares fit to three points for three temperatures, $T = 17.5$ K, 18 K, and 22 K. The resistivity for $T = 18$ K and 22 K are presented in Fig. 4.5, so the agreement between one of the data points and the real measurements is not shown and the other two fits and measurements are not in a very good agreement. By this method they find $b = 1$.

Using the reported value for ω_p^* and the reported value of A, where $\rho(T) = \rho_0 + AT^2$, I estimated T_0=103 K. This makes their measurement in the right temperature range. However their signal to noise is poor at low frequency, as can be observed in the Fig. 4.5(B) where many of their optical measurements are inconsistent with the dc measurements. This raises doubt about the validity of b based on those data points. The paper by Nagel *et al.* also cites a value $b = 2.5$ for a measurement on chromium by another group [3]. In the original paper no attempt was made to obtain the value for b, and Nagel *et al.* appears to have obtained this value from their conductivity measurement at temperature 320 K. As I mentioned in the previous section, FLT is valid at low temperatures, so its applicability to room temperature measurements is open to question.

Material	T_{max}(meV)	ω_{max}(meV)	b	Source
UPt_3	1	1	< 1	[26]
$Ce_{.95}Ca_{.05}TiO_{3.04}$	25	100	1.72	[13]
Cr	28	370	2.5	[3]
$Nd_{.95}TiO_4$	24	50	1.1	[29]
URu_2Si_2	2	10	1	[20]

Table 4.2: Summary of experimental studies to determine the prefactor b, for some heavy fermions, compiled by Nagel *et al.* [20].

4.4.7 Terahertz spectroscopy of MnSi

In the next chapter I will discuss our THz-TDS measurements of a thin MnSi film for the frequency range 0.1 THz to 1.0 THz and temperature range T=6.5-290 K. With the THz-TDS technique, the complex conductivity is acquired directly, without using Kramer-Kronig analysis, so it is more accurate than conventional optical methods. By applying the procedure that I described earlier in this section, we found T_0=180 K. For the temperature range T<180 K, we have enough data to conclusively test FLT. Fig. 4.2 shows our frequency

and temperature range in comparison with the other work discussed here. Fig. 4.6 shows the $\Re e(\sigma^{-1})$ as a function of frequency for three selected temperatures and the fits to Eq. 4.1. As the temperature decreases, the value of b increases, and at the lowest temperature, $T = 6.5$ K, we estimate $b = 3.88 \pm 0.23$, consistent with the FLT prediction. As I will discuss, systematic uncertainties limit the strength of this conclusion, so further work will still be necessary to test FLT fully. If confirmed, this is possibly the first observation of Fermi liquid frequency-temperature conductivity scaling in a metal.

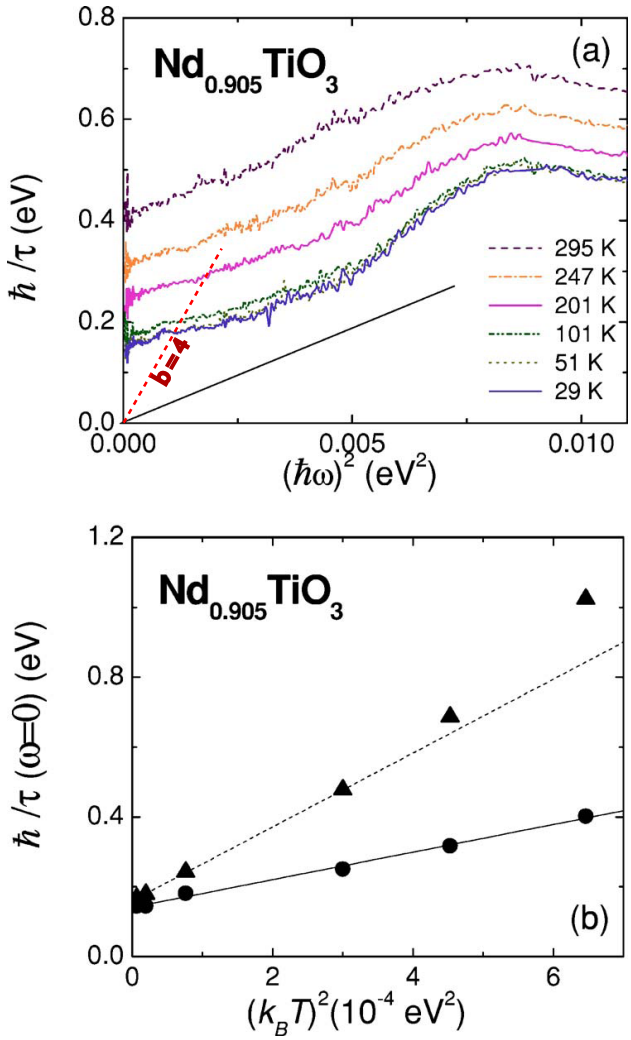

Figure 4.4: (a) The scattering rate $(\hbar/\tau)$ as a function of $(\hbar\omega)^2$ at various temperatures. The solid line shows a least-squares fit to the room-temperature data. (b) Closed circles show the dc value of the scattering rate as a function of temperature squared. The solid line is a least squares fit to the closed circles. The solid triangles show the dc scattering rate obtained from the direct dc measurements of the resistivity and the dashed line is the linear fit to it. The large dashed line is where $b = 4$. From Yang *et al.* [29].

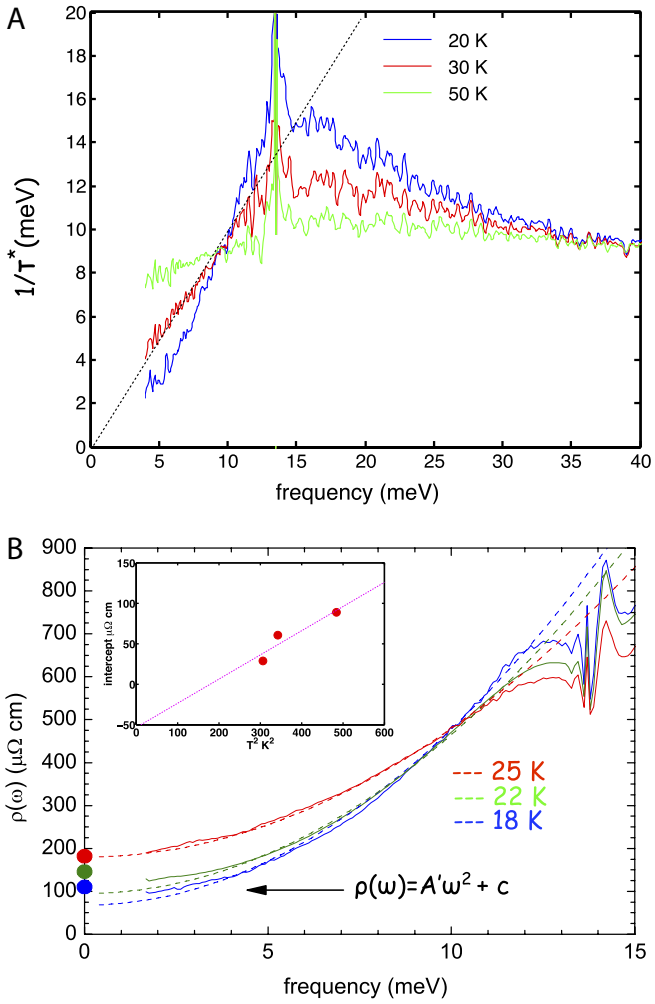

Figure 4.5: (A) Scattering rate of URu_2Si_2 as a function of frequency for three different temperatures. The dashed line is $1/\tau^* = \omega$ (B) The optical resistivity as a function of frequency for three different temperatures. Solid lines are the data and dashed lines are the fit to a parabolic equation with A' and $c(T)$ as fit parameters. The inset of the plot is the $c(T)$ as a function of T^2 for three temperatures T= 17.5 K, 18 K, 22 K. From Nagel *et al.* [20].

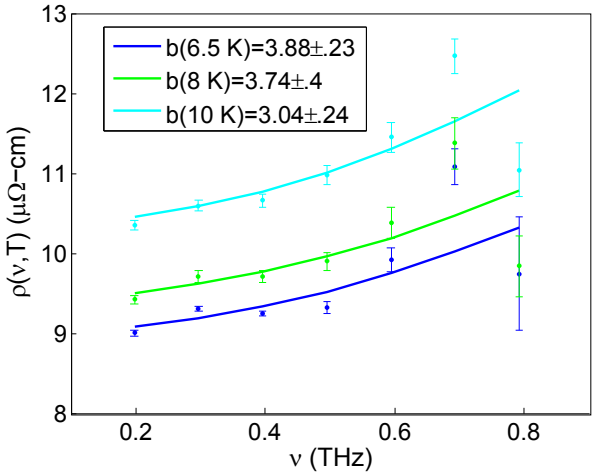

Figure 4.6: The resistivity of MnSi as a function of frequency for three selected temperatures. Dots are data points and solid lines is the fit to Eq.4.1.

Chapter 5

THz time-domain spectroscopy of MnSi films

In this chapter, I present the results from our THz-TDS measurements on a thin film of MnSi. From the optical conductivity measurements, we extract other physical properties like the scattering lifetime, resistivity and plasma frequency. At low temperatures and low frequencies, the conductivity is consistent with the prediction of FLT, $\rho(\omega, T) = [\sigma(\omega, T)]^{-1} = \rho_0 + A[(\hbar\omega)^2 + (2\pi k_B T)^2]$.

5.1 Basic facts about MnSi

MnSi is a remarkably well studied material. It crystallizes in the B20 structure, depicted in Fig 5.1, and exhibits a helically ordered magnetic ground state. An intense interest has been focused on its properties as a function of pressure, where it exhibits a quantum phase transition from a helimagnetic phase to a non magnetic phase. Fig. 5.2 shows the temperature pressure phase diagram of MnSi, where different colors correspond to different phases. The phase diagram shows that at low pressures and low temperatures, the Fermi liquid behavior dominates and as the temperature increases the non-Fermi liquid behavior dominates, and as the pressure increase MnSi goes to the paramagnetic phase [22]. Although most of the interest on MnSi is focused at its behavior as a function of temperature, even at the ambient pressure it exhibits unusual behaviors. As depicted in Fig. 5.3, the conductivity has a very sharp peak at low temperature, which rolls over much more gradually than one would expect

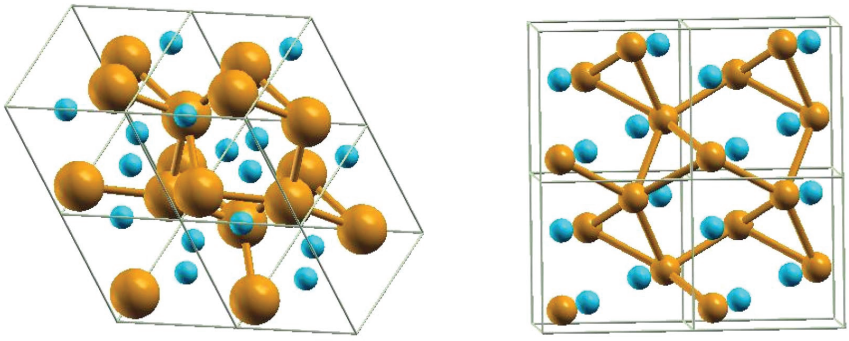

Figure 5.1: Two views of the B20 crystal structure of MnSi, showing four cubic cells. The larger atoms are Mn and smaller ones are Si. Right: a view along the (111) direction. Left: view along the (100) direction. From Jeong *et al.* [11].

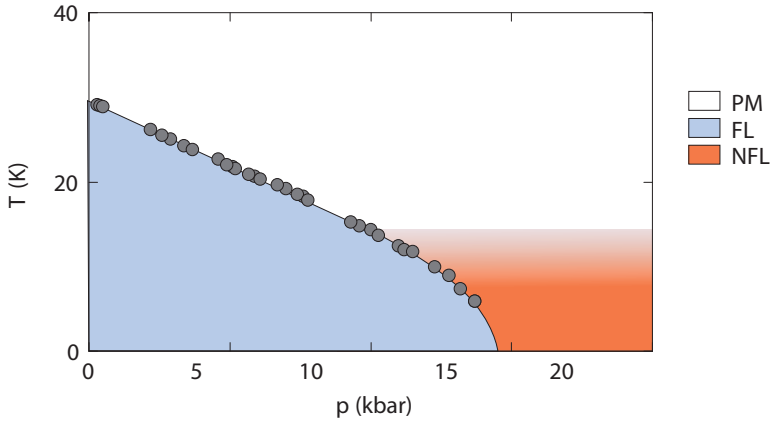

Figure 5.2: Temperature-pressure phase diagram of MnSi. PM corresponds to the paramagnetic region, FL corresponds to the region that Fermi liquid behavior is valid and NFL corresponds to the region that Fermi liquid behavior is no longer observed. From Ritz *et al.* [22].

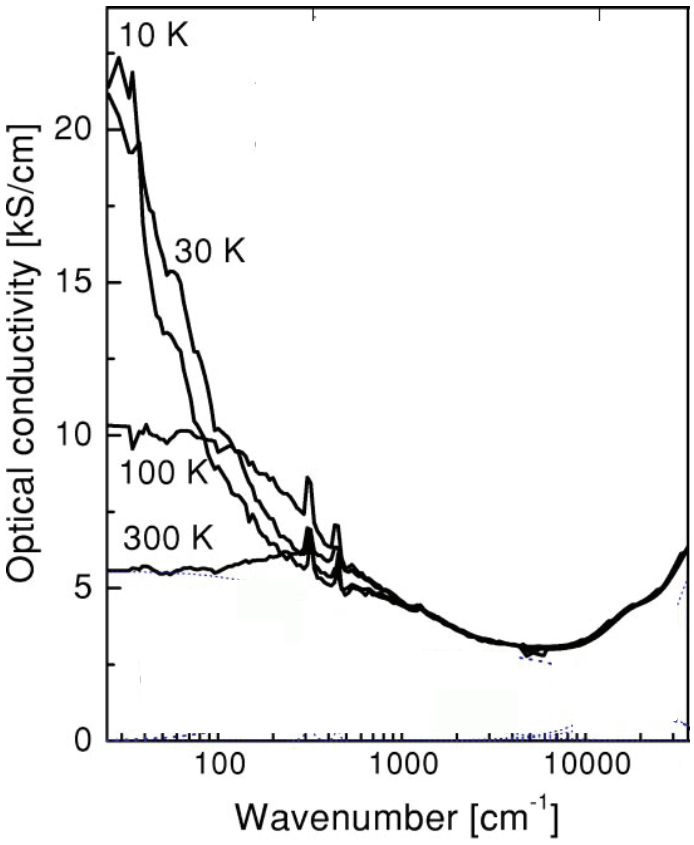

Figure 5.3: Optical conductivity of MnSi at four different temperatures. From Mena *et al.* [17].

from a conventional Drude model. This was pointed out by Mena *et al.*, and they suggested this behavior is an evidence for physics beyond Fermi liquid theory [17]. Using infrared spectroscopy, they showed that the conductivity of MnSi follows an anomalous power law form:

$$\tilde{\sigma}(\omega) = \frac{\sigma(0)}{(1 - i\omega\tau)^{\alpha}}, \tag{5.1}$$

with $\alpha = 0.5$. For $\alpha = 1$ this general form reduces to the Drude conductivity.

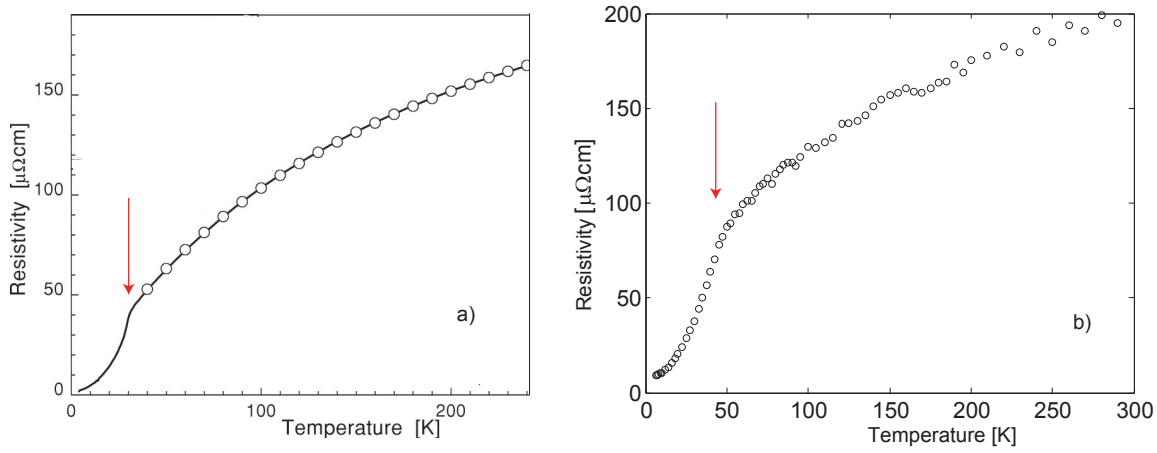

Figure 5.4: a) Dc resistivity of a single crystal of MnSi as a function of temperature, from Mena *et al.* [17]. b) Dc resistivity of a thin film of MnSi as a function of temperature. The red arrow indicates the point of transiton from the helimagnetic phase to non magnetic phase. The transition temperature for the single crystal is at 30 K, while for the thin film is at 50 K.

5.2 THz-TDS on MnSi

5.2.1 Sample preparation

Ted Monchesky and his former PhD student Eric Karhu from Dalhousie university provided the MnSi sample. This film is 25 nm and is grown epitaxially on a high resistivity Si(111) wafer. The final MnSi film is a result of co-deposition of Mn and Si by the molecular beam epitaxy (MBE) method [28]. The high quality of the film was reflected in the residual resistivity ratio which was above 25. The phase transition temperature of MnSi is noticeably different between thin films and single crystals, as a result of the strain induced by the substrate. This difference can be observed in Fig. 5.4 that shows the dc measurement of a single crystal and a thin film side by side, with arrows to indicate their transition temperatures. In the single crystal the transition temperature is $T_c \simeq 30$ K , while for the thin film it is $T_c \simeq 40$ K.

5.2.2 Conductivity spectra

We use THz-TDS to measure the frequency-dependent conductivity for the temperature range T=6.5-290 K. The results of our measurements are shown in Fig. 5.5. The colour of the curves changes from blue to red, where blue corresponds to the lowest temperature and the red corresponds to the highest temperature. We restrict our fits to the frequency range 100-900 GHz, where the signal to noise ratio is best. At low temperatures, σ_1 falls rapidly with the frequency while at higher temperatures, it becomes nearly independent of the frequency. As this occurs, σ_2 rises rapidly from $\sigma_2(\omega = 0) = 0$ at low temperatures, but develops a weakly negative slope at high temperatures. I will discuss the influence of the significance of this negative slope in Sec. 5.2.4.

Fig. 5.5.c) and Fig. 5.5 d) show the Drude fit to the conductivity data for selected temperatures. There is good agreement between the conductivity at lower temperatures and the Drude fit. This is supported by Fig. 5.6, which shows the value of α obtained from direct fits of Eq. 5.1 to the conductivity spectra in Fig. 5.5. When α is allowed to vary, the best fit is close to the value found by Mena *et al.* at higher frequencies [17], but it approaches $\alpha = 1$ as the temperature is lowered. As we will see in Sec. 5.2.3, our measurement shows that $\alpha \neq 1$ at temperatures for which the resistivity still satisfies the T^2 dependence. We leave this puzzling observation as an open question.

5.2.3 Resistivity

The temperature dependent dc resistivity for T=6.5-290 K is shown in Fig. 5.7. The dc resistivities measured optically and by four-point probe method are shown. We obtain good agreement between the two methods, if we scale the four-point measurement results by 1.08. This is justified as there is some uncertainty associated with the contact resistance and size. Note that, apart from the overall scale, the two measurements have identical temperature dependence. Our results show a kink in the temperature dependent resistivity at $T = 50$ K, signaling a phase transition. This corresponds to a transition from a helimagnetic state to a paramagnetic state at this temperature. Below 50 K, we fit the resistivity to $\rho(T) = \rho(0) + aT^{\mu}$ to obtain $\rho(0) = 7.02 \pm 1.10\,\mu\Omega\,\mathrm{cm}$, $a = 0.03\,\mu\Omega\,\mathrm{cm\,K^{-1.97}}$ and $\mu = 1.97 \pm 0.10$. The results are consistent with $\mu = 2$, the FLT prediction.

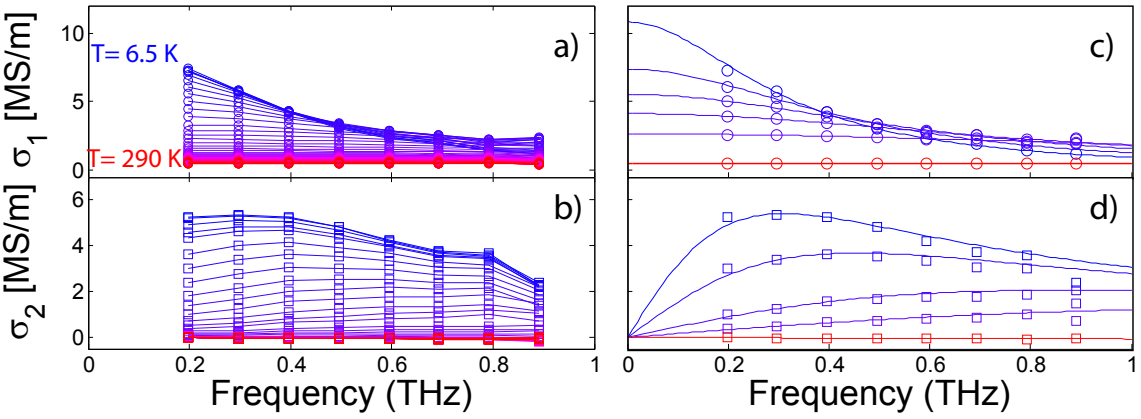

Figure 5.5: Conductivity as a function of frequency for temperature range T=6.5-290 K. a) and b) are the real and imaginary part of the measured conductivity, respectively. The temperature increment is not the same for the entire range. The temperature increments are: 1 K for 6-10 K, 2 K for 10-20 K, 2.5 K for 20-100 K, 5 K for 100-200 K and 10 K for 200-290 K. c) and d) are the real and imaginary part of the Drude fit to the conductivity for temperatures T=6.5 K, 14 K, 18 K, 22.5 K, 30 K and T=200 K. The markers are the data points and solid lines are the fits. In this figure the error bars are smaller than markers, so we just show markers.

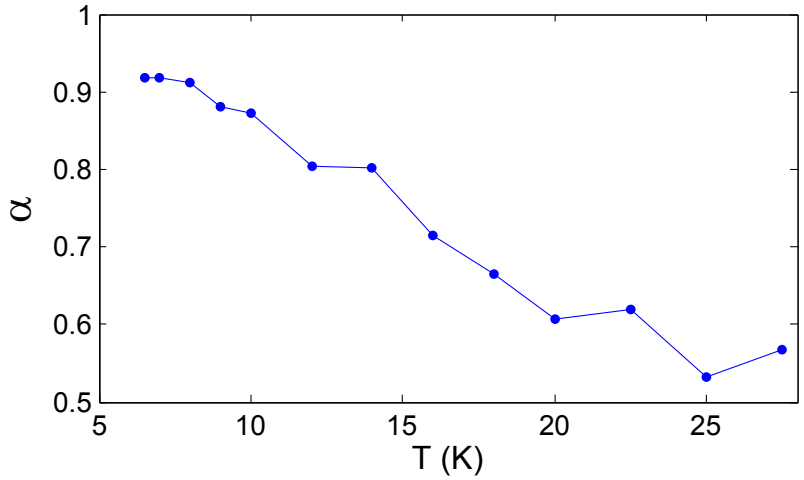

Figure 5.6: α as a function of temperature. At low temperatures α approaches 1.

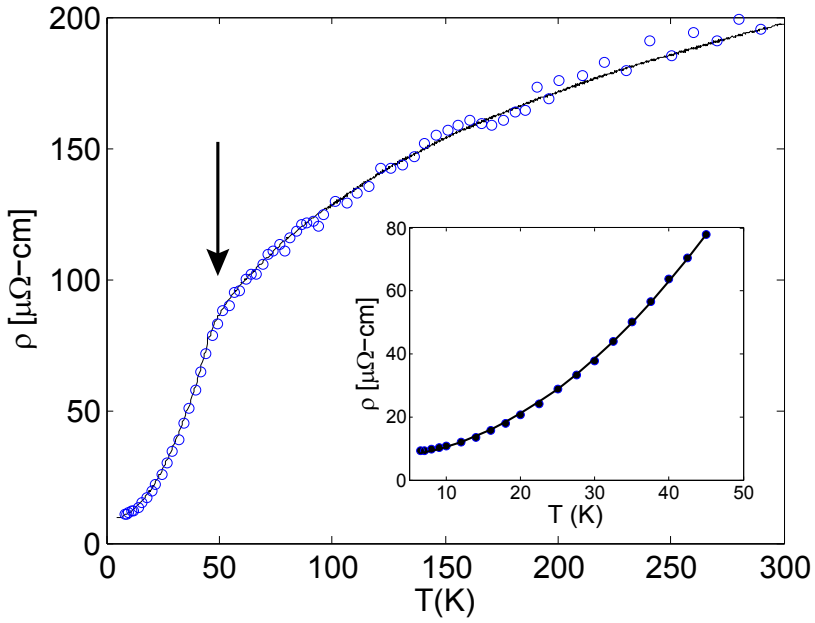

Figure 5.7: Dc resistivity as a function of temperature. Circles represent the temperature dependent dc resistivity obtained by optical measurements. Solid line shows the four-point resistivity measurement, scaled up by a factor of 1.08. Bottom right inset: dots are the dc resistivity below 50 K and the solid line is the fit to $\rho(T) = aT^{\mu} + \rho(0)$, as described in the text.

5.2.4 Relaxation time

For materials that exhibit Drude behavior,

$$\tilde{\sigma}(\omega) = \frac{\sigma_0}{1 - i\omega\tau}, \tag{5.2}$$

the slope of $\sigma_2(\omega)$ gives us a direct measure of the Drude scattering lifetime τ:

$$\lim_{\omega\to 0} \frac{1}{\sigma_0}\frac{d\sigma_2}{d\omega} = \tau. \tag{5.3}$$

If we take Eq. 5.3 as the *definition* of τ, we can use the Kramers-Kronig relations to obtain a general relationship between τ and $\sigma_1(\omega)$,

$$\tau = \frac{2}{\pi}\int_0^\infty \frac{1 - \sigma_1(\omega')/\sigma_0}{\omega'^2} d\omega'. \tag{5.4}$$

Hence, τ is related to a weighted integral of the curvature of σ_1. We use Eq. 5.4 as the general operational definition of τ. To see how τ behaves when σ_1 deviates from the Drude form, we examine Eq. 5.4 for the sum of a Drude and Lorentzian peak,

$$\tilde{\sigma}(\omega) = \frac{\sigma_0}{1 - i\omega\tau} - \frac{i\omega\epsilon_0\Omega}{\omega_0^2 - \omega^2 - i\gamma\omega}, \tag{5.5}$$

where γ and Ω are positive. The value of τ calculated using Eq. 5.4 for this generalized conductivity could yield negative results. This is due to the strong upward curvature in the conductivity that can not always be outweighed by the positive contribution from higher frequencies. Although, a negative scattering lifetime appears to be non-physical at first sight, this upward curvature in the conductivity is a sign of developing a pseudo-gap. Mena *et al.* observed this behavior in optical conductivity measurements of MnSi as shown in Fig. 5.3. The figure shows an upward curvature in the conductivity at T=300 K. Fig. 5.8 demonstrates how a negative τ can potentially arise from the generalized conductivity model. Fig. 5.8 (a)-(c) shows the steps in the calculation of τ starting from, Eq. 5.2, the Drude conductivity relation, while Fig. 5.8 (d)-(f), shows the same calculation for the modified Drude conductivity in Eq. 5.5. Comparing, Fig. 5.8(c) and 5.8(f), we observe that in the case of the Drude conductivity, the function flattens out and falls as $1/\omega^2$ at high frequencies. Consequently, the conductivity is a Lorentzian centered at the zero frequency with an amplitude of τ^2 and a width of $1/\tau$ with an area of $\pi\tau/2$ which is always positive. Fig. 5.8(f) shows the integrand of the operational definition of τ as a function of frequency, for the generalized conductivity. The curvature at zero frequency is negative, dominating

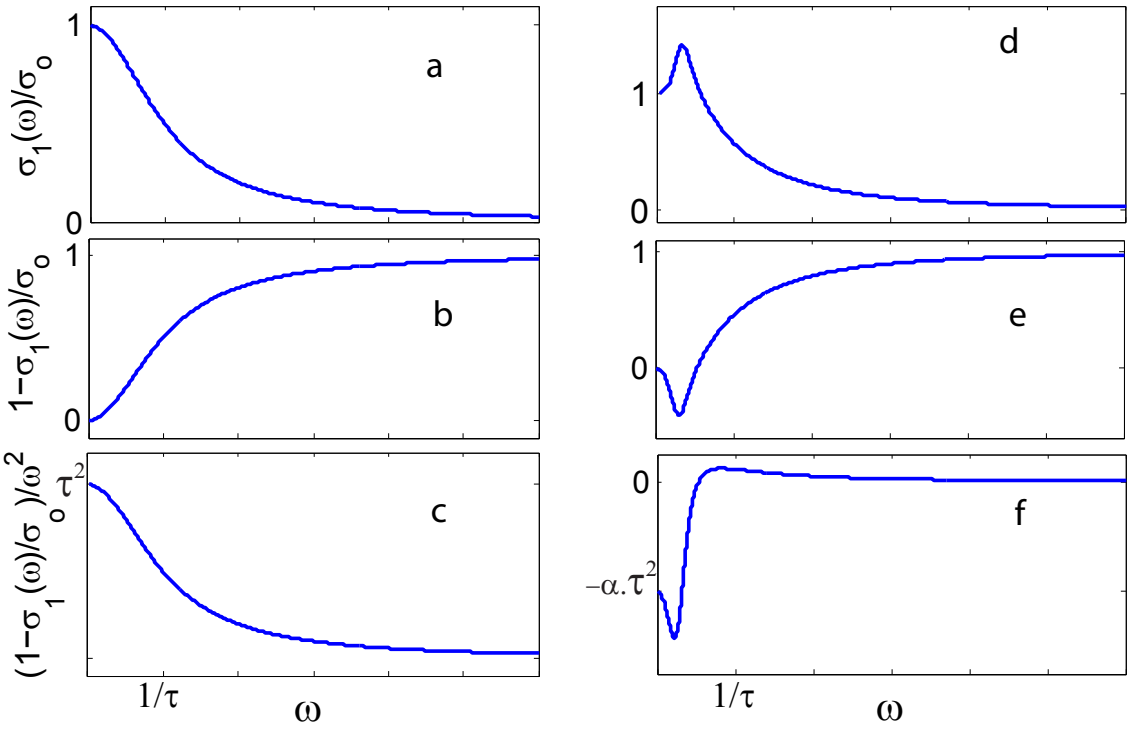

Figure 5.8: Step by step comparison between obtaining the scattering lifetime for Drude like and more general form of conductivity. Fig. 5.8a to c is the process of obtaining τ for the Drude like conductivity and Fig. 5.8d to f is the process of obtaining τ for a more general form of conductivity, Eq. 5.5. Fig. 5.8a and d show the shape of σ_1/σ_0, part b and e shows how $1-\sigma_1/\sigma_0$ look like and part c and f are $\frac{1-\sigma_1/\sigma_0}{\omega}$ as a function of frequency.

the positive contributions coming from the higher frequencies, for which the amplitude is suppressed by $1/\omega^2$. This can produce a negative value for τ.

Fig. 5.9 shows a measurement of τ determined in this way, as a function of temperature. At the lowest temperature, a large scattering lifetime is observed that drops dramatically as it reaches the critical temperature of 50 K. Above the critical temperature, τ becomes negative, which is an indication of upward curvature in $\sigma_1(\omega)$ near $\omega = 0$ that we attribute to a pseudo-gap in the density of states.

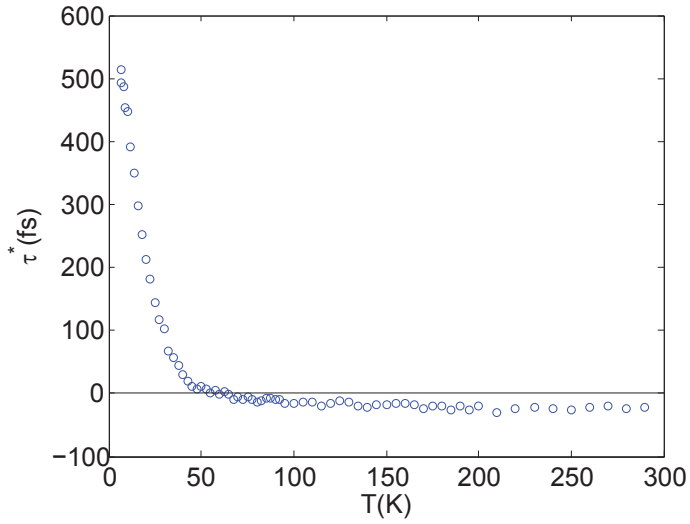

Figure 5.9: Scattering life time as a function of temperature. At the lowest temperature we have a huge scattering lifetime, half a picosecond that decreases at higher temperatures, and becomes negative.

5.2.5 Plasma frequency

From measurements of the relaxation time and resistivity we can determine the plasma frequency ω_p, a fundamental ground-state property of the Fermi surface is given by:

$$\omega_p^{-2} = \epsilon_0 \rho \tau, \tag{5.6}$$

where ρ is the dc resistivity, τ is the scattering life time, and ϵ_0 is the free space permittivity. Fig. 5.10 shows the result of the temperature dependent plasma frequency measurements. At low temperatures where we believe the conductivity has the Drude format, the plasma frequency saturates at about 1 eV, while at higher temperatures where conductivity is not Drude like, the plasma frequency can not be inferred. Preliminary band theory calculations give $\omega_p = 2.34$ eV [23], which allows us to estimate the mass renormalization due to interactions beyond the band theory framework:

$$\frac{m^*}{m_b} = \left(\frac{\omega_p}{\omega_p^*}\right)^2 = 5.5, \tag{5.7}$$

where ω_p^* corresponds to our measured plasma frequency and m_b and ω_p correspond to the value from band theory calculations.

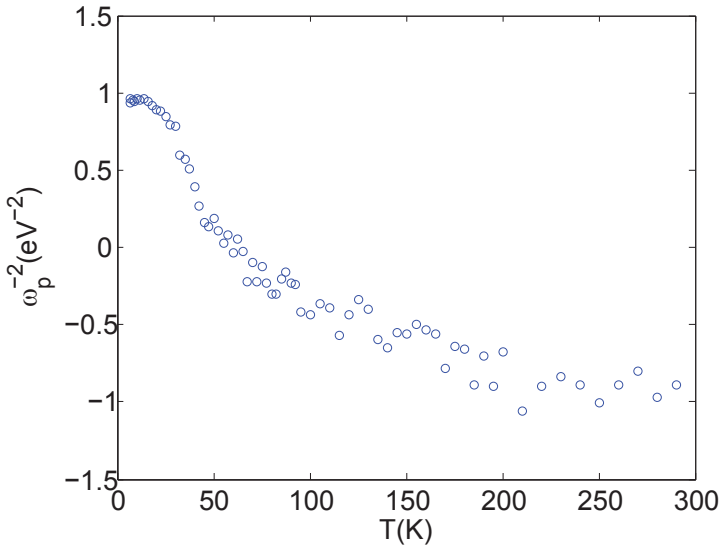

Figure 5.10: Plasma frequency as a function of temperature. At low temperatures the conductivity follows the Drude model, plasma frequency is 1 eV.

5.2.6 Frequency-temperature scaling parameter

One of the goals of this work is to test Fermi liquid theory experimentally for thin films of MnSi. There has been some debate in the literature on whether or not MnSi follows FLT. Here, we measure the temperature dependence of the resistivity and compare it to the FLT prediction,

$$\rho(\omega, T) = \rho_0 + A[(\hbar\omega)^2 + b(\pi k_B T)^2], \tag{5.8}$$

where, FLT predicts b=4 [10]. As I discussed in Ch. 4, estimates of b made for various compounds presumed to follow FLT have not been consistent with this prediction. However, as we have access to lower frequencies compared to previous works, we can estimate b well within the regime of validity for FLT. A suitable compound for this study is MnSi, as good quality thin films can be grown. This is essential for our measurements. Additionally, there has been some debates in the literature [17] on whether or not it follows FLT which makes MnSi an interesting case to study.

The details of our analysis procedure are described in Chapter 3. In summary, in the frequency domain, we fit the ratio of a reference pulse (i.e. through a substrate) to a sample pulse (i.e. through a thin film on a substrate) to Eq. 3.5, a rational polynomial function

with polynomials of degree (1,1). This is equivalent to a transfer function corresponding to the Drude model, Eq. 3.9. From this fit, we determine τ and ρ_0, the scattering life-time and dc resistivity respectively. The same procedure can be performed by fitting the transfer function to a rational polynomial with polynomials of degree (2,2). Here the parameter b is related to the coefficient of the second order parameter in the denominator.

Inside the cryostat, we have three separate apertures installed on a motorized stage. At any time, one of the apertures can be moved behind the cryostat window so that it is aligned with the propagation direction of the terahertz pulse. As I discussed in Sec. 3.2.3, to tackle the systematic uncertainties associated with our measurements at low temperatures, we follow the following procedure. The sample is mounted on the middle aperture while two reference substrates are mounted on the remaining apertures. At each temperature, we perform pairs of reference/sample measurements, once with the bottom reference substrate, and again with the top reference substrate. This is to characterize and account for the potential systematic differences associated with the sample holder position.

Fig. 5.11 shows the results of the two measurements and their average. We plot $1/b$ versus temperature because the random error in this quantity is relatively constant, which causes the random error in b to diverge when $1/b \to 0$. The dotted line corresponds to the FLT prediction of $1/b = 1/4$. At low temperatures, the estimate of $1/b$ from the averaged measurements is consistent with the prediction of the FLT, then increases to unity at higher temperatures. However, this change is also correlated with a divergence between the two measurements, indicating a potentially large systematic error from the sample positioner.

In the very near future we will be working to eliminate this source of uncertainty to obtain a more rigorous test of FLT. However, if we assume the average is the correct value of b, Fig. 5.12 shows the resistivity spectrum as a function of frequency for different temperature. Measured frequency-dependent resistivities are plotted along with the b values that are obtained from the rational polynomial fit.

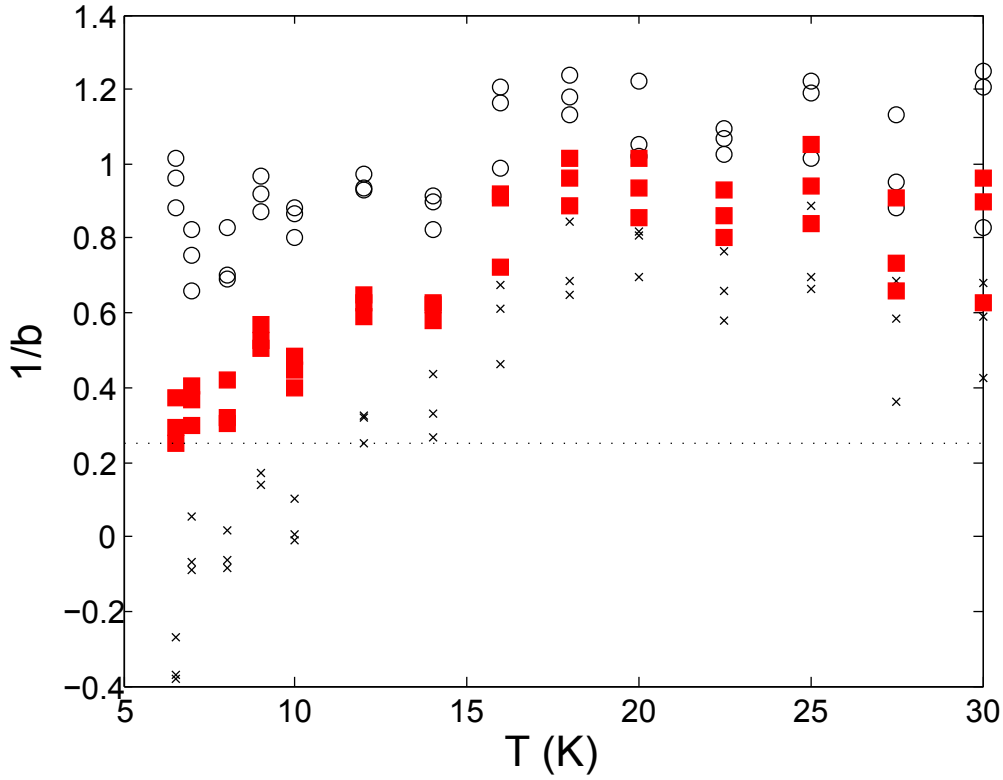

Figure 5.11: Estimated $1/b$ as a function of temperature. ◯ corresponds to the measurement where the bottom substrate is the reference, × corresponds to the measurements where the top substrate is the reference, solid squares correspond to the average of these two, and the dotted line is where $1/b = 1/4$.

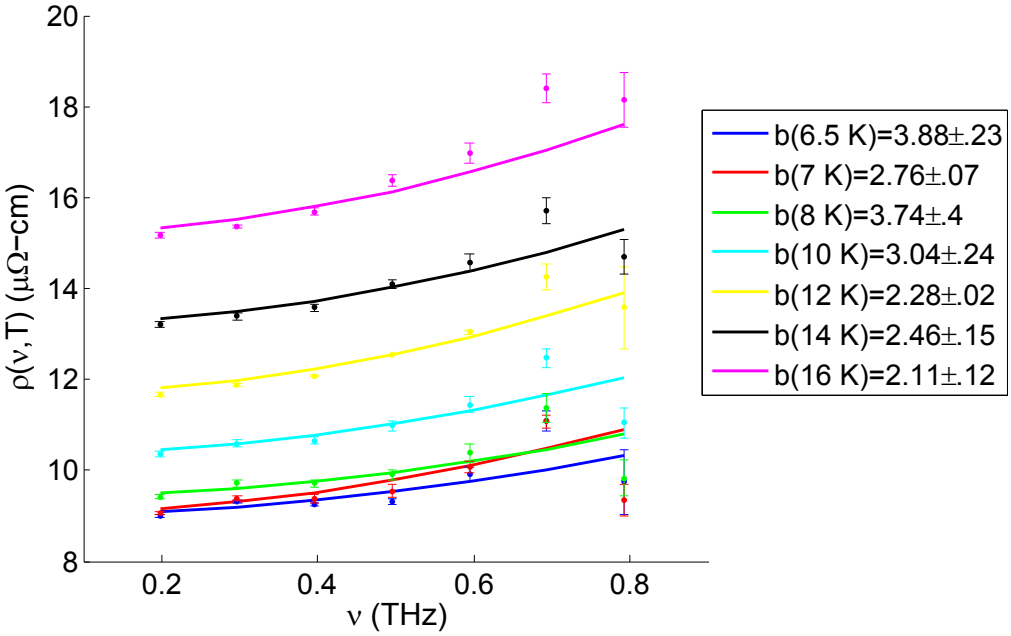

Figure 5.12: The frequency dependent resistivity at different temperatures. The points are the data and the solid line is $\rho(\omega, T)$ with b that is determined by averaging the two b's that we obtained .

Chapter 6

Conclusions and future directions

We have used THz-TDS to measure the dynamical conductivity of a thin film of MnSi over a temperature range T= 6.5 - 290 K. From fits to the Drude form at low frequencies, we obtain ρ_0 and τ as a function of temperature. We find good agreement between the optically measured resistivity and that measured by a four-point probe technique. Both measurements show a kink at T≈50 K which is the transition point between the helimagnetic phase and the non magnetic phase. At the lowest temperature, the value of τ reaches 0.5 ps, but drops dramatically as temperature increases and takes a negative value for temperatures above 50 K. The negative value is an indication of a pseudogap at higher temperatures. At the lowest temperatures, the plasma frequency saturates at 1 eV, which gives a mass renormalization of about 5.5 when compared with the plasma frequency obtained from band theory calculations.

One of the main goals of this thesis was to test the FLT prediction and for the universal function of resistivity, $\rho(\omega, T) = A[(\hbar\omega)^2 + b(k_B T)^2]$. We find that $b \simeq 4$, consistent with FLT for the lowest temperature, with significant systematic uncertainty. This value of b decreases as the temperature increases, and for T>20 K, approaches 1. To improve the systematic uncertainty in the system, we are planning to replace the Mylar windows of the cryostat with sapphire windows. We believe that the source of uncertainty at low temperatures is the optical path length sensitivity of Mylar to small temperature fluctuations in the cryostat. The optical path length of sapphire does not show such a large sensitivity to temperature. After changing the windows we expect to be able to measure the value of b more reliably.

Bibliography

[1] N. W. Ashcroft and N. D. Mermin. *Solid State Physics*. Brooks/Cole, Pacific Grove, 2009.

[2] D. H. Auston., K. P. Cheung, and P.R. Smith. Picosecond photoconductiong hertzian dipoles. *Appl. Phys. Lett.*, 45:284–286, 1984.

[3] D. N. Basov, E. J. Singley, and S. V. Dordevic. Sum rules and electrodynamics of high-T_c cuprates in the pseudogap state. *Phys. Rev. B*, 65:054516, 2002.

[4] C. Berthod, J. Mravlje, X. Deng, R. Žitko, D. van der Marel, and A. Georges. Non-Drude universal scaling laws for the optical response of local Fermi liquids. *Phys. Rev. B*, 87:115109, 2013.

[5] S. L. Dexheimer, editor. *Terahertz Spectroscopy Principle and Applications*. CRC Press, Boca Raton, 2008.

[6] A. D. Farahani. *Terahertz conductivity measurements on chromium-vanadium alloys and photoexcited insulating cuprates.* PhD thesis, Simon Fraser University, 2011.

[7] M. A. Gilmore, S. Kamal, D. M. Broun, and J. S. Dodge. Determination of electron-phonon interaction parameters from time-domain terahertz spectroscopy. *Appl. Phys. Lett*, 88:141910, 2006.

[8] D. J. Griffiths. *Introduction to Electrodynamics*. Prentice Hall, Upper Saddle River, 1999.

[9] D. Grischkowsky, Søren Keiding, Martin Exter, and Ch. Fattinger. Far-infrared time-domain spectroscopy with terahertz beams of dielectrics and semiconductors. *J. Opt. Soc. Am. B*, 7:2006–2015, 1990.

[10] R.N. Gurzhi. Mutual electron correlations in metal optics. *Sov. Phys. JETP*, 35:673–675, 1959.

[11] T. Jeong and W. E. Pickett. Implications of the B20 crystal structure for the magnetoelectronic structure of MnSi. *Phys. Rev. B*, 70:075114, 2004.

[12] E. Karhu, S. Kahwaji, T. L. Monchesky, C. Parsons, M. D. Robertson, and C. Maunders. Structure and magnetic properties of mnsi epitaxial thin films. *Phys. Rev. B*, 82:184417, Nov 2010.

[13] T. Katsufuji and Y. Tokura. Frequency and temperature dependence of conductivity for perovskite titanates. *Phys. Rev. B*, 60:7673–7676, 1999.

[14] C. P. Kubler. *Creation and characterization of a Terahertz time domain spectrometer.* Master's thesis, Simon Fraser University, 2002.

[15] G. B. Lea. *Metallic scattering lifetime measurements with terahertz time-domain spectroscopy.* Master's thesis, Simon Fraser University, 2010.

[16] D. L. Maslov and A. V. Chubukov. First-Matsubara-frequency rule in a Fermi liquid. I. Optical conductivity and comparison to experiment. *Phys. Rev. B*, 86:155137, 2012.

[17] F. P. Mena, D. van der Marel, A. Damascelli, M. Fäth, A. A. Menovsky, and J. A. Mydosh. Heavy carriers and non-Drude optical conductivity in MnSi. *Phys. Rev. B*, 67:241101, 2003.

[18] S. I. Mirzaei, D. Stricker, J. N. Hancock, C. Berthod, A. Georges, E. v. Heumen, M. K. Chan, X. Zhao, Y. Li, M. Greven, N. Barii, and D. van der Marel. Spectroscopic evidence for fermi liquid-like energy and temperature dependence of the relaxation rate in the pseudogap phase of the cuprates. *Proceedings of the National Academy of Sciences*, 2013.

[19] P. Mousavi, F. Haran, D. Jez, F. Santosa, and J. S. Dodge. Simultaneous composition and thickness measurement of paper using terahertz time-domain spectroscopy. *Appl. Opt.*, 48(33):6541–6546, 2009.

[20] U. Nagel, T. Uleksin, T. Room, R. P. S. M. Lobo, P. Lejay, C. C. Homes, J. S. Hall, A. W. Kinross, S. K. Purdy, T. Munsie, T. J. Williams, G. M. Luke, and T. Timusk. Optical spectroscopy shows that the normal state of URu_2Si_2 is an anomalous Fermi liquid. *PNAS*, 109:19161–19165, 2012.

[21] D. Pines and P. Nozieres. *The Theory Of Quantum Liquids.* W. A. Benjamin, New York, 1966.

[22] R. Ritz, M. Halder, M. Wagner, C. Franz, A. Bauer, and C. Pfleiderer. Formation of a topological non-Fermi liquid in MnSi. *Nature*, 497:231234, 2013.

[23] U. Roessler. Private communication, 2012.

[24] D. G Sahota. *Statistical Data Analysis Techniques for Terahertz Time Domain Spectroscopy.* BSc thesis, Simon Fraser University, 2007.

[25] P. R. Smith, D. H. Auston, and M. C. Nuss. Subpicosecond photoconducting dipole antennas. *IEEE J. Quantum Electron.*, 24:255–260, 1988.

[26] P. E. Sulewski, A. J. Sievers, M. B. Maple, M. S. Torikachvili, J. L. Smith, and Z. Fisk. Far-infrared absorptivity of UPt_3. *Phys. Rev. B*, 38:5338–5352, 1988.

[27] M. Tinkham. Energy gap interpretation of experiments on infrared transmission through superconducting films. *Phys. Rev.*, 104:845–846, 1956.

[28] M. N. Wilson, E. A. Karhu, A. S. Quigley, U. K. Rößler, A. B. Butenko, A. N. Bogdanov, M. D. Robertson, and T. L. Monchesky. Extended elliptic skyrmion gratings in epitaxial MnSi thin films. *Phys. Rev. B*, 86:144420, 2012.

[29] J. Yang, J. Hwang, T. Timusk, A. S. Sefat, and J. E. Greedan. Temperature-dependent optical spectroscopy studies of $Nd_{1-x}TiO_3$. *Phys. Rev. B*, 73:195125, 2006.